

# The 9 and 18 Micron Luminosity Function of Various Types of Galaxies with AKARI: Implication for the Dust Torus Structure of AGN

Yoshiki TOBA<sup>1,2</sup>, Shinki OYABU<sup>3</sup>, Hideo MATSUHARA<sup>2</sup>, Matthew A MALKAN<sup>4</sup>, Daisuke ISHIHARA<sup>3</sup>, Takehiko WADA<sup>2</sup>, Youichi OHYAMA<sup>5</sup>, Satoshi TAKITA<sup>2</sup>, and Chisato YAMAUCHI<sup>6</sup>

<sup>1</sup>*Department of Space and Astronautical Science, the Graduate University for Advanced Studies (Sokendai), 3-1-1 Yoshinodai, Chuo-ku, Sagamihara, Kanagawa 252-5210*

*toba@ir.isas.jaxa.jp*

<sup>2</sup>*Institute of Space and Astronautical Science, Japan Aerospace Exploration Agency, 3-1-1 Yoshinodai, Chuo-ku, Sagamihara, Kanagawa 252-5210*

<sup>3</sup>*Graduate School of Science, Nagoya University, Furo-cho, Chikusa-ku, Nagoya, Aichi 464-8602*

<sup>4</sup>*Department of Physics and Astronomy, University of California, Los Angeles, CA 90095-1547, USA*

<sup>5</sup>*Institute of Astronomy and Astrophysics, Academia Sinica, P.O. Box 23-141, Taipei 10617, Taiwan, R.O.C*

<sup>6</sup>*Astronomy Data Center, National Astronomical Observatory of Japan, 2-21-1 Osawa, Mitaka, Tokyo 181-8588*

(Received 2012 August 22; accepted 2013 July 20)

## Abstract

We present the 9 and 18  $\mu\text{m}$  luminosity functions (LFs) of galaxies at  $0.006 \leq z \leq 0.8$  (with an average redshift of  $\sim 0.04$ ) using the AKARI mid-infrared all-sky survey catalog. We selected 243 galaxies at 9  $\mu\text{m}$  and 255 galaxies at 18  $\mu\text{m}$  from the Sloan Digital Sky Survey (SDSS) spectroscopy region. These galaxies were then classified by their optical emission lines, such as the line width of  $\text{H}\alpha$  or by their emission line ratios of  $[\text{OIII}]/\text{H}\beta$  and  $[\text{NII}]/\text{H}\alpha$  into five types: Type 1 active galactic nuclei (AGN) (Type 1); Type 2 AGN (Type 2); low-ionization narrow emission line galaxies (LINER); galaxies with both star formation and narrow-line AGN activity (composite galaxies); and star-forming galaxies (SF). We found that (i) the number density ratio of Type 2 to Type 1 AGNs is  $1.73 \pm 0.36$ , which is larger than a result obtained from the optical LF and (ii) this ratio decreases with increasing 18  $\mu\text{m}$  luminosity.

**Key words:** galaxies: active — galaxies: luminosity function, mass function — galaxies: nuclei — infrared: galaxies

## 1. Introduction

The unified model for active galactic nuclei (AGN) postulates that Type 1 and Type 2 AGNs are intrinsically identical. The most popular explanation for their observed differences is due to different viewing orientations (Antonucci 1993, Urry & Padovani 1995). A geometrically thick dusty torus is supposed to surround the AGN central engine. When an observer views the central region near the polar axis of the torus, a broad emission line region (BLR) can be observed directly, identifying these galaxies as Type 1 AGNs. On the other hand, at angles near the equatorial plane of the torus, the central region of the AGN, with its BLR, cannot be observed. The narrow emission line region (NLR), the size of which is at least an order of magnitude larger than the torus, is always observed regardless of torus orientation. Thus, these galaxies are classified as Type 2 AGNs.

The key parameters of dust torus unification—the intrinsic geometry (e.g., thickness and covering factor) and physical properties—are still unknown. To investigate these parameters, infrared (IR) observations of AGNs are important, because the reprocessed radiation from the dust in the torus is re-emitted in the IR wavelength range. In this study, we focus on the geometrical covering fraction of the dust torus. The covering factor (CF) is defined as the fraction of the sky, as seen from the AGN center, which is blocked by obscuring material. This corresponds to the fraction of Type 2 AGNs out of the entire AGN population. Many previous studies have attempted to estimate CF. For instance, Mor, Netzer, & Elitzur (2009) estimated CF for 26 luminous quasars. They fitted the  $\sim 2\text{-}35\ \mu\text{m}$  spectra from the Spitzer Space Telescope (Werner et al. 2004) IRS using three-component models made of a clumpy torus, dusty NLR clouds, and very hot dust clouds. The clumpy torus model attempts to fix problems with torus unification. In this more complicated model, the observed differences between Type 1 and Type 2 AGNs are due not only to orientation, but also to random probability (Nenkova et al. 2008a, Nenkova et al. 2008b). The observer’s line-of-sight passing through the torus may, with some probability, pass through a gap in the clouds. Such an object is classified as a Type 1 AGN, even though it is viewed at a high inclination angle, similar to other Type 2 AGNs. Conversely, even when viewed from a near-polar angle, there is some small probability that a dust cloud may happen to obscure the AGN along the particular sightline. Such an object is classified as Type 2 AGN. This complex model in general lacks the simplicity and predictive power of the original dusty torus. Those authors found a mean CF value of 0.27 by fitting the AGN data, which may be anti-correlated with bolometric luminosity. Alonso-Herrero et al. (2011) also calculated the CF of 13 nearby Seyfert galaxies by using clumpy torus models with a Bayesian approach to fit their IR spectral energy distributions (SEDs) and ground-based high-angular-resolution mid-IR spectroscopy. They found a tendency for the CF to be lower ( $\sim 0.1\text{-}0.3$ ) at high AGN luminosities than at low AGN luminosities ( $\sim 0.9\text{-}1$ ), which supports the result of Mor, Netzer, & Elitzur (2009).

However, these studies were limited to small numbers of individual objects, rather than a statistically complete AGN sample. To overcome this problem, we estimate the CF of dust torus using the IR luminosity function (LF). The LF of galaxies is a fundamental statistical tool for describing galaxy properties, since it should be almost entirely independent of the viewing angle. In this study, we construct the LF using the AKARI satellite. AKARI, the first Japanese space satellite dedicated to infrared astronomy, was launched in 2006 (Murakami et al. 2007). One of its most important results was an all-sky survey in the mid-IR (MIR) and far-IR (FIR) (Ishihara et al. 2010, Yamamura et al. 2010). The spatial resolution and sensitivity of AKARI are much better than those of the Infrared Astronomical Satellite (IRAS: Neugebauer et al. 1984, Beichman et al. 1988) which performed a previous all-sky IR survey. In particular, the detection limits ( $5\sigma$ ) for point sources per scan are 50 and 90 mJy for the 9 and 18  $\mu\text{m}$  bands, respectively, with spatial resolutions of about  $5''$ , thus surpassing the IRAS survey in its 12 and 25  $\mu\text{m}$  bands by an order of magnitude in both sensitivity and spatial resolution.

In this study, we report the 9 and 18  $\mu\text{m}$  LFs of galaxies at  $0.006 \leq z \leq 0.8$  using the AKARI MIR all-sky survey catalog. The sample selection is described in section 2. In section 3, we present the 9 and 18  $\mu\text{m}$  LFs with the  $1/V_{\text{max}}$  technique and compare our results with previous studies. In section 4, we discuss the number density ratio of Type 1 AGNs and Type 2 AGNs as estimated from the LFs of AGNs and compare it to previous optical and X-ray estimates. This study provides us with an important estimate of the dust torus structure of AGNs. Throughout this study, we assume a flat universe with  $\Omega_k = 0$ , and we adopt  $(\Omega_M, \Omega_\Lambda) = (0.3, 0.7)$  and  $H_0 = 75 \text{ km s}^{-1} \text{ Mpc}^{-1}$ .

## 2. Data and Analysis

### 2.1. Sample Selection

The AKARI MIR all-sky survey catalog provides the positions and fluxes of 870,973 sources (including 844,649 sources in the 9  $\mu\text{m}$  band and 194,551 sources in the 18  $\mu\text{m}$  band). The sample used for this study was selected from AKARI MIR sources with spectroscopy from the Sloan Digital Sky Survey (SDSS) Data Release 7 (Abazajian et al. 2009) and the Center for Astrophysics (CfA) redshift survey (ZCAT: Huchra et al. 1995). The flow chart used for sample selection is shown in figure 1. First, our sample was narrowed to the 29,418 AKARI sources in the SDSS spectroscopic region. To ensure flux accuracy, we then extracted objects that met the following criteria:

- flux (9  $\mu\text{m}$ )  $\geq 90$  mJy (for 9  $\mu\text{m}$  LF)
- flux (18  $\mu\text{m}$ )  $\geq 170$  mJy (for 18  $\mu\text{m}$  LF)

These fluxes correspond to the 50% completeness flux limits calculated by Kataza et al. (2010). Next the 25,139 remaining objects (24,936 sources with 9  $\mu\text{m}$  flux greater than 90 mJy and 4,316 sources with 18  $\mu\text{m}$  flux greater than 170 mJy) were cross-matched with the Tycho-

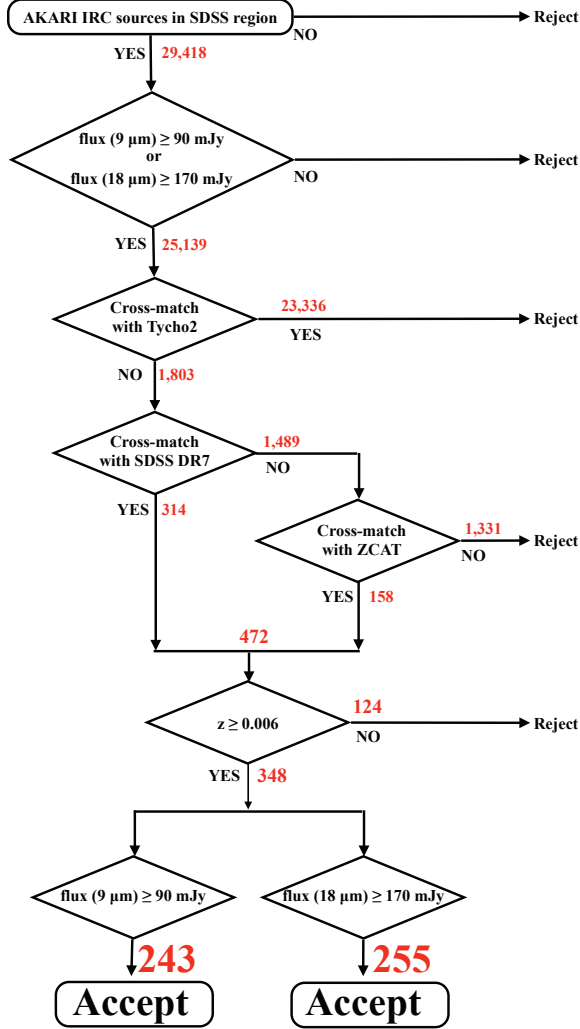


Fig. 1. Flow chart for sample selection process.

2 Catalog (Høg et al. 2000) to remove the galactic bright stars. This catalog contains the positions, proper motions, and two-color photometry for the 2.5 million bright stars in the sky down to the magnitude limit of the plates ( $V_T \sim 11.5$ ). To avoid the omission of high proper-motion stars, we referred to the *mean position*, rigorously propagated to the epoch J2000.0, by the proper motions in this catalog. As a result, a total of 23,336 ( $\sim 92.8\%$  of the objects cross-identified with the Tycho-2 catalog) stars (hereinafter AKARI-Tycho 2 objects) were extracted. As shown in figure 2, we adopted 3 arcsec as our search radius, because the star density in the SDSS spectroscopic region is at most  $\sim 50 \text{ deg}^{-1}$  (Høg et al. 2000). Thus, by adopting this search radius, the probability of chance coincidence is less than 0.01% (i.e.,  $25,139 \times 0.0001 \sim 3$  sources may be misidentified), which is acceptable.

We then identified 1,803 AKARI sources in the SDSS spectroscopic catalog and in the ZCAT. Both have the redshifts of  $\sim 900,000$  objects cataloged. The SDSS spectroscopic catalog

mainly contains magnitude-limited objects with Petrosian (1976) magnitude brighter than  $r = 17.77$  for galaxy samples (Strauss et al. 2002) and with point-spread function (PSF) magnitude brighter than  $i = 19.1$  for quasar samples at  $z \leq 2.3$  (Richards et al. 2002). The advantage of using the SDSS is that we obtain uniform spectroscopic data. The average redshift of these spectroscopic objects is  $\sim 0.1$ . However, bright objects that might be saturated are excluded in the spectroscopic target selection (Eisenstein et al. 2001, Strauss et al. 2002). Therefore, for bright galaxies, we use the ZCAT, which is compiled from literature, and has a limiting magnitude of  $\sim 15.5$  in the B band. The search radii for the SDSS and ZCAT were 6 and 12 arcsec, respectively, as shown in figure 2. For the SDSS, the surface density of galaxies in the SDSS spectroscopic region is  $92 \text{ deg}^{-2}$  (Strauss et al. 2002). Within 6 arcsec around each AKARI MIR source, the expected number of galaxies is then 0.008. Adopting this search radius means that the probability of chance coincidence is less than 0.1% (i.e.,  $1,803 \times 0.001 \sim 2$  sources may be misidentified), which is acceptable. For the ZCAT, the surface density of galaxies in the SDSS spectroscopic region is  $\sim 71 \text{ deg}^{-2}$ . Thus, by adopting a search radius of 12 arcsec, the probability of chance coincidence is less than 0.25% for the AKARI-ZCAT sources (i.e.,  $1,489 \times 0.0025 \sim 4$  sources may be misidentified). This value is relatively larger than the corresponding value of the SDSS, but is acceptable, because the ZCAT assembles the nearby or spatially extended galaxies. At this point, 472 galaxies remained for selection. Furthermore, we excluded 124 local galaxies with  $z \leq 0.006$  from the sample. The errors in distance measurement are dominated by peculiar motions for galaxies with  $z \leq 0.006$ , and thus, the luminosity also has a large error. A final sample of 348 galaxies was selected. The mean value of their redshifts is 0.04, and the redshift distribution is shown in figure 3. The details of the 348 galaxies selected are given in table 1. Ultimately, 243 and 255 galaxies were selected for construction of the  $9 \mu\text{m}$  LF and the  $18 \mu\text{m}$  LF, respectively. Throughout this process, we mainly used the AKARI Catalog Archive Server (Yamauchi et al. 2011a) and a software kit called “2MASS Catalog Server Kit” to easily construct a high-performance database server for the Two Micron All Sky Survey (2MASS) Point Source Catalog (which includes 470,992,970 objects) and several all-sky catalogs (Yamauchi 2011b).

## 2.2. Classification of Spectroscopic Galaxy Type

We classified the 243 and 255 galaxies into the following five types by using the line width of  $\text{H}\alpha$  or the emission line ratios of  $[\text{OIII}]/\text{H}\beta$  and  $[\text{NII}]/\text{H}\alpha$ , as shown in figure 4: Type 1 AGNs (Type1); Type 2 AGNs (Type 2); low-ionization narrow emission line galaxies (LINER); galaxies that are likely to contain both star formation and AGN activity (composite types of galaxies, hereinafter Composite); and star-forming galaxies (SF).

First, we separated the Type 1 objects using the full-width at half-maximum (FWHM) of the  $\text{H}\alpha$  emission line. The FWHM was estimated by the following relation:

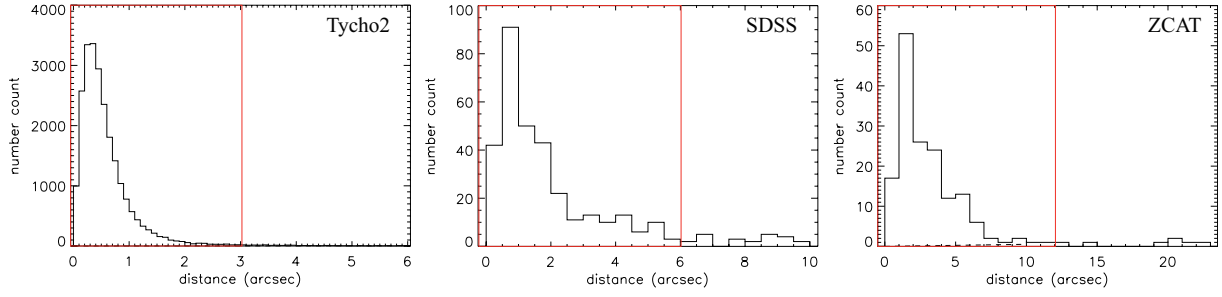


**Fig. 2.** Histogram of the angular separation of AKARI sources from the Tycho 2 (left), SDSS (middle), and ZCAT (right) coordinates. We adopt search radii for the Tycho 2, SDSS, and ZCAT as 3, 6, and 12 arcsec, respectively. The red frame represents the search radii used.

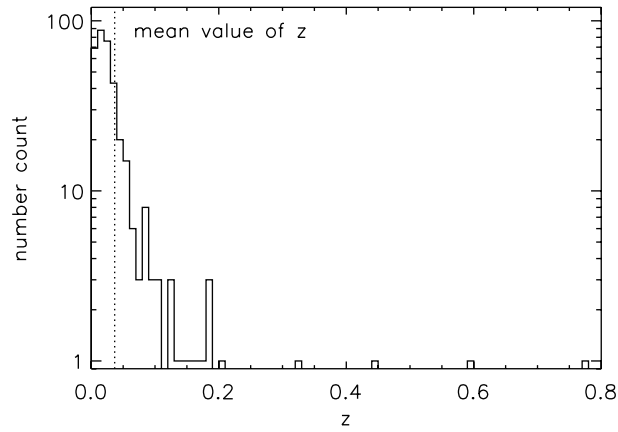


**Fig. 3.** Redshift distribution of the 348 selected galaxies. The mean value of redshift is represented by the dotted line.

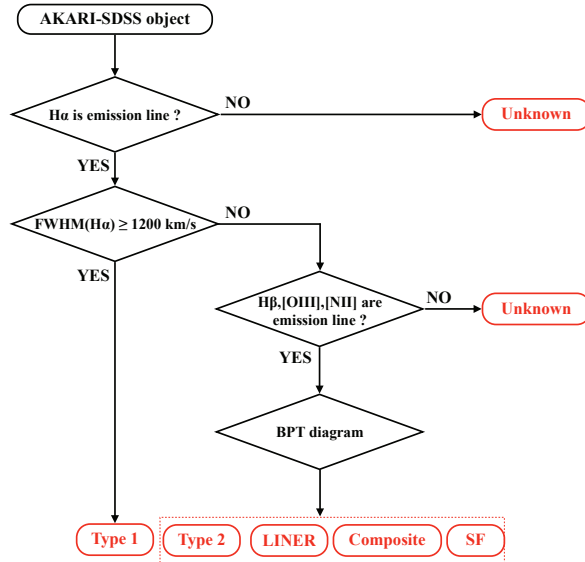


**Fig. 4.** Outline of the type classification process.

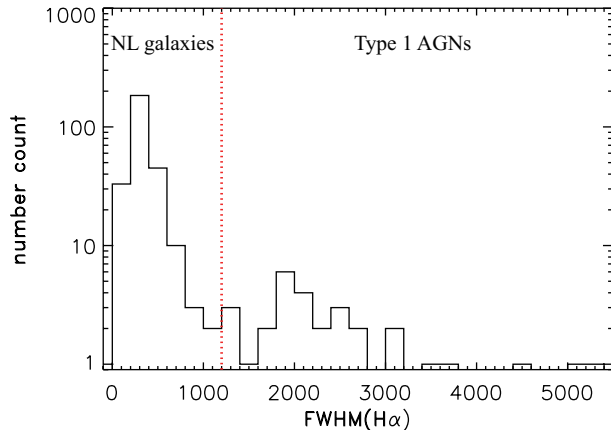


**Fig. 5.** Distribution of the full-width at half-maximum (FWHM) of  $H\alpha$  for AKARI-SDSS galaxies. We selected objects with an  $\text{FWHM}(H\alpha)$  greater than  $1200 \text{ km s}^{-1}$  as Type 1 AGNs. Narrow emission line galaxies (NL galaxies) were defined as having an  $\text{FWHM}(H\alpha)$  smaller than  $1200 \text{ km s}^{-1}$  in this study.

$$\text{FWHM}(H\alpha) = \frac{2.35\sigma c}{\lambda_0(1+z)}, \quad (1)$$

where  $\sigma$  is the variance of the Gaussian curve that fits the  $H\alpha$  emission line,  $c$  is the speed of light, and  $\lambda_0$  is the rest-frame wavelength of the  $H\alpha$  line ( $6563 \text{ \AA}$ ). The values of  $\sigma$  and  $z$  were obtained from the “sigma” and “z” columns, respectively, in the SDSS DR7 `SpecLine` table. For ZCAT galaxies, we classified Type 1 according to the previous literature, because the ZCAT does not contain spectroscopic line information. Figure 5 gives the distribution of the FWHM values of the  $H\alpha$  emission line. The distribution is bimodal with a minimum at  $1200 \text{ km s}^{-1}$ , as reported by Hao et al. (2005a). They established the criterion of  $\text{FWHM}(H\alpha) \geq 1200 \text{ km s}^{-1}$  for identifying broad-line AGNs from spectroscopic SDSS data. Similarly, we extracted objects with an  $\text{FWHM}(H\alpha)$  greater than  $1200 \text{ km s}^{-1}$  as Type 1. Next, objects that have  $H\alpha$  emission with an  $\text{FWHM} \leq 1200 \text{ km s}^{-1}$  were classified as Type 2, LINER, Composite, or SF by using the optical flux line ratios of  $[\text{OIII}]\lambda 5007/H\beta$  versus  $[\text{NII}]\lambda 6583/H\alpha$  (BPT diagram suggested by Baldwin et al. 1981), as shown in figure 6. These line fluxes were estimated by  $\sqrt{2\pi}\sigma h$ , where  $h$  is the height of the Gaussian curve that fits each emission line. The  $h$  values were obtained from the “height” column in the SDSS DR7 `SpecLine` table. In this study, we did not correct the effect of stellar absorption. The ZCAT galaxies were also classified as Type 2, LINER, SF, or Composite according to previous literature. However, some galaxies were not classified, because (i)  $H\alpha$ ,  $H\beta$ ,  $[\text{OIII}]$  or  $[\text{NII}]$  were not detected (neither in absorption nor emission) in the SDSS, and (ii) no spectroscopic type was available in the literature. These galaxies are classified as unknown types of galaxies (hereinafter, “Unknown”).

The final classification of each of the 243 and 255 galaxies are summarized in table 2. As shown in table 2, the  $9 \mu\text{m}$  LF sample has 25 Type 1s, 39 Type 2s, 6 LINERs, 50 Composites, 95 SFs, and 28 Unknowns. The  $18 \mu\text{m}$  LF sample has 41 Type 1s, 64 Type 2s, 11 LINERs, 57 Composites, 71 SFs, and 11 Unknowns. These results strongly confirm the finding of Spinoglio

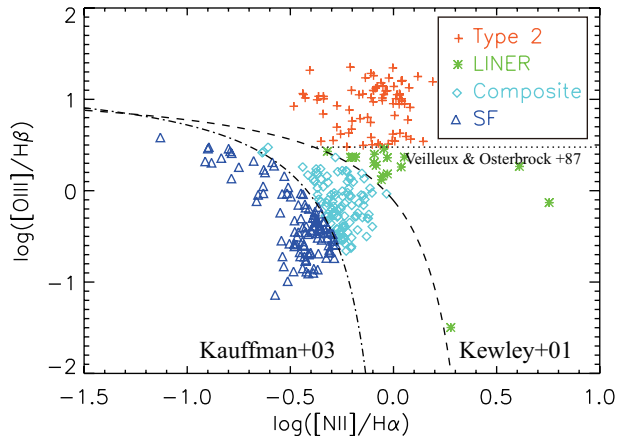


**Fig. 6.** BPT diagram plotting the emission-line flux ratio  $[\text{NII}]/\text{H}\alpha$  versus  $[\text{OIII}]/\text{H}\beta$  for all the NL galaxies in which the line flux information is available. The dashed-dotted line is the criterion given by Kauffmann et al. (2003), the dashed line is the criterion given by Kewley et al. (2001), and the dotted line is the traditional scheme (see for example, Veilleux & Osterbrock 1987).

& Malkan (1989) that MIR selection strongly favors finding galaxies with active nuclei because of their strong nuclear emissions from heated dust grains. In their pioneering study using IRAS, they found that 15% of 12  $\mu\text{m}$ -selected galaxies are AGNs. Our selection using AKARI is even more efficient, containing  $\sim 26\%$  and 41% AGNs (Type 1 + Type 2 AGNs) in the 9 and 18  $\mu\text{m}$  LF samples, respectively. This is due to AKARI's improved ability to isolate nuclear point-source emission in the MIR. Spinoglio & Malkan's 12  $\mu\text{m}$  sample, on the other hand, was based on *total* fluxes measured by IRAS, which typically include emissions over a few square arcminutes. This much coarser spatial resolution substantially dilutes the infrared signal of the active nucleus. A secondary disadvantage of the IRAS 12  $\mu\text{m}$  bandpass was that it included a strong potential for contributions from polycyclic aromatic hydrocarbon (PAH) emissions, which are unrelated to the presence of an active nucleus.

Table 2 also indicates that the 18  $\mu\text{m}$  band is especially powerful for finding AGNs. The detection rate of AGNs in the 18  $\mu\text{m}$  band (41%) is higher than that in the 9  $\mu\text{m}$  band ( $\sim 26\%$ ), since the 9  $\mu\text{m}$  sample is also affected by PAH contributions in the same way as the 12  $\mu\text{m}$  sample as mentioned above. Figure 7 presents the flux distributions at 9  $\mu\text{m}$  and 18  $\mu\text{m}$ . The distributions of 9 and 18  $\mu\text{m}$  luminosities as a function of redshift are illustrated in figure 8. For the flux distribution, there is no specific difference between each type of galaxy shown in figure 7. In contrast, for the redshift distribution, the Type 2s and especially the Type 1s have higher redshifts than the others.

### 2.3. Completeness Correction

#### 2.3.1. $V/V_{\text{max}}$ test

Before constructing LFs, we performed the standard  $V/V_{\text{max}}$  test (Schmidt 1968) to examine whether the spatial distribution of the sources in a sample is uniform. Here  $V$  is the



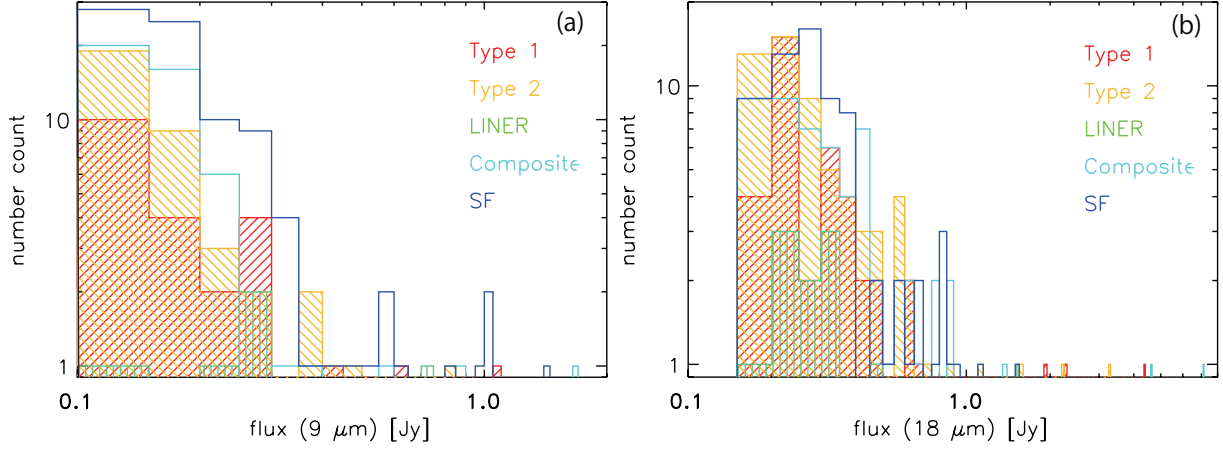


**Fig. 7.** Flux distribution for each type of galaxy at (a) 9  $\mu\text{m}$  and (b) 18  $\mu\text{m}$ .

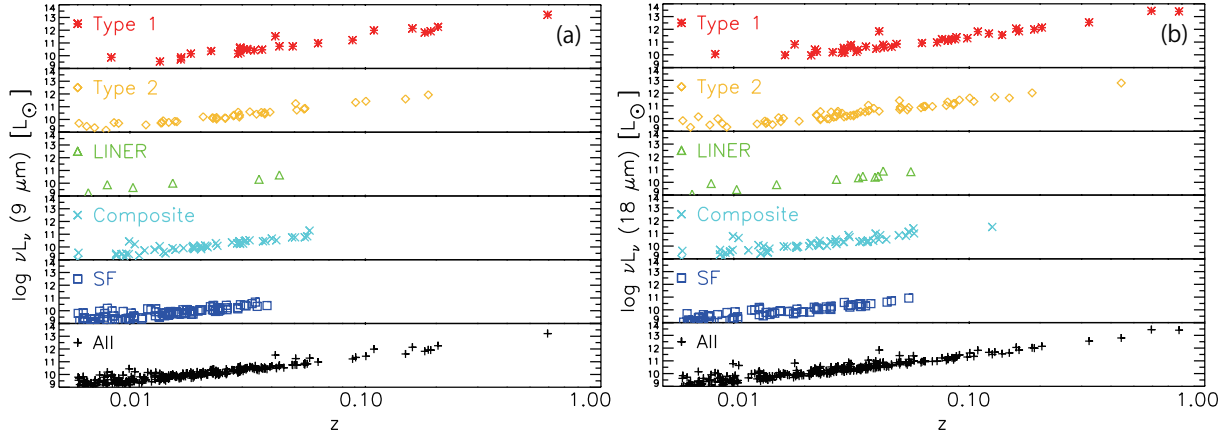


**Fig. 8.** (a) 9  $\mu\text{m}$  and (b) 18  $\mu\text{m}$  luminosities as a function of redshift for each type of galaxy.

volume enclosed at the redshift of an object, and  $V_{\text{max}}$  is the volume that would be enclosed at the maximum redshift at which the object could be detected. If the sample is complete, the mean value of  $V/V_{\text{max}}$  should be 0.5.

In the context of the cosmology we adopted,  $V$  and  $V_{\text{max}}$  are described as

$$V(z) = \frac{c}{H_0} \int_{\Omega} \int_{z_{\text{min}}}^z C(z') \frac{(1+z')^2 D_A^2}{\sqrt{\Omega_M(1+z')^3 + \Omega_\Lambda}} dz' d\Omega, \quad (2)$$

$$V_{\text{max}}(z) = \frac{c}{H_0} \int_{\Omega} \int_{z_{\text{min}}}^{z_{\text{max}}} C(z') \frac{(1+z')^2 D_A^2}{\sqrt{\Omega_M(1+z')^3 + \Omega_\Lambda}} dz' d\Omega, \quad (3)$$

where  $D_A$  is the angular distance for a given redshift in our adopted cosmology,  $\Omega$  is the solid angle of the SDSS spectroscopic region (8032 deg<sup>2</sup>), and  $z_{\text{min}} = 0.006$  (see section 2.1) is the lower limit of the redshift bin considered.  $z_{\text{max}}$  is the maximum redshift at which the object could be seen, given the flux limit of the sample.

However,  $z_{\text{max}}$  cannot be solved analytically; hence, we calculated  $z_{\text{max}}$  numerically as

follows. Using the luminosity  $L_\nu$  of the source at the redshift  $z$ , the observed flux  $f_\nu$  is described as follows:

$$f_\nu(z) = \frac{(1+z)^{1-\alpha}}{4\pi D_L^2(z)} L_\nu, \quad (4)$$

where  $D_L$  is the luminosity distance for a given redshift in our adopted cosmology. The spectral index  $\alpha$  is derived from the assumption that the SED of the galaxies in the infrared obeys a simple power law  $f(\nu) \propto \nu^{-\alpha}$ . When a source is artificially moved away until the detection limit  $f_\nu(z_{\max}) = f_{\min,\nu}$ , equation (4) becomes

$$f_{\min,\nu} = \frac{(1+z_{\max})^{1-\alpha}}{4\pi D_{L_{\max}}^2} L_\nu, \quad (5)$$

where  $D_{L_{\max}}$  is the maximum luminosity distance  $D_L(z_{\max})$ . Using equations (4) and (5), the maximum luminosity distance can be derived as

$$D_{L_{\max}} = D_L \left( \frac{1+z}{1+z_{\max}} \right)^{\frac{\alpha-1}{2}} \left( \frac{f_\nu}{f_{\min,\nu}} \right)^{\frac{1}{2}}. \quad (6)$$

On the other hand, the luminosity distance  $D_L$  is defined as

$$D_L = \frac{c}{H_0} (1+z) \int_0^z \frac{dz'}{\sqrt{\Omega_M(1+z')^3 + \Omega_\Lambda}}. \quad (7)$$

Hence,  $D_{L_{\max}}$  also can be described as

$$D_{L_{\max}} = \frac{c}{H_0} (1+z_{\max}) \int_0^{z_{\max}} \frac{dz'}{\sqrt{\Omega_M(1+z')^3 + \Omega_\Lambda}}. \quad (8)$$

Therefore, we numerically estimate  $z_{\max}$  by substituting  $z$  into equations (6) and (8) at intervals of  $\Delta z$  and iterating the above approach until the difference between the  $D_{L_{\max}}$  values obtained from equations (6) and (8) is minimized. In this study, we used  $\Delta z = 10^{-5}$ .

We note that the spectral index  $\alpha$  is calculated using the 9  $\mu\text{m}$  and 18  $\mu\text{m}$  fluxes as

$$\alpha = -\frac{\log\left(\frac{f_{18}}{f_9}\right)}{\log\left(\frac{\nu_{18}}{\nu_9}\right)}. \quad (9)$$

Although the distribution of  $\alpha$  has large scatter, the average value  $\langle \alpha \rangle$  is  $1.08 \pm 0.68$  for all samples. The average  $\langle \alpha \rangle$  slopes of Type 1s, Type 2s, and Composites are relatively large ( $\geq 1$ ). Conversely,  $\langle \alpha \rangle$  for SFs is relatively small ( $\leq 1$ ). LINERs have an intermediate value ( $\sim 1$ ). In this study, we calculate  $\langle \alpha \rangle$  for each type of galaxy, and when an object is missing  $f_{18}$  or  $f_9$  information, we adopt these values, taking into account its type.

Next, we determine the completeness correction function  $C(z)$ . First, we construct the dependence of completeness  $C(f)$  for flux  $f$  using the result of the log N-log S test described by Kataza et al. (2010). Second, we convert the flux to the redshift for each object using equation (4). Here  $L_\nu$  is treated as a constant for each object, because the luminosity of an object does not change when an object is artificially moved away with redshift. Figure 9 shows

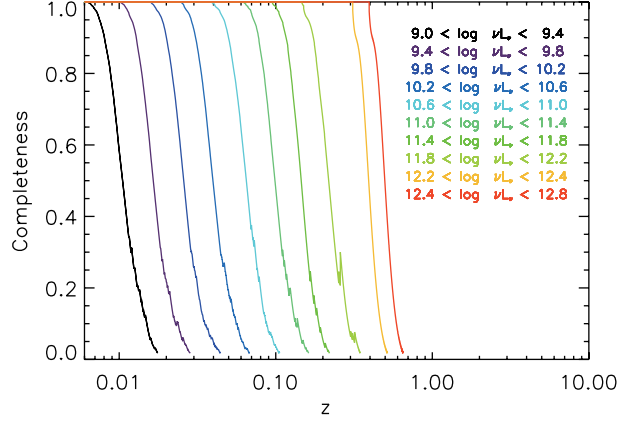


**Fig. 9.** Averaged completeness as a function of redshift for 18  $\mu\text{m}$  galaxies.

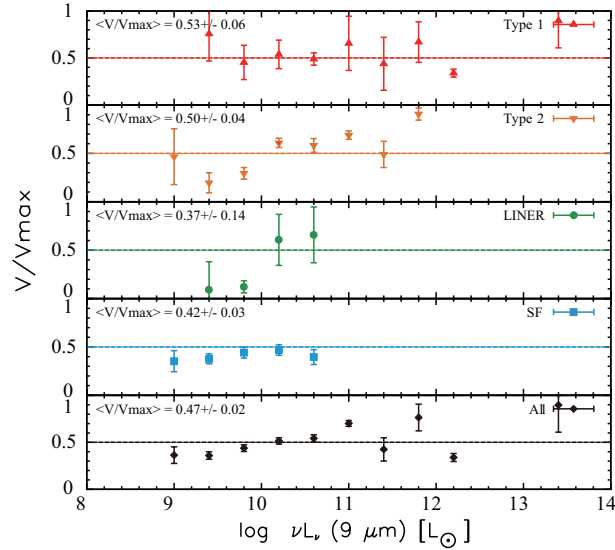


**Fig. 10.** Average values of  $V/V_{\text{max}}$  for the different types of galaxies as a function of 9  $\mu\text{m}$  luminosity.

the averaged completeness as a function of the redshift for each 18  $\mu\text{m}$  luminosity bin.

Figures 10 and 11 show the results of the  $V/V_{\text{max}}$  tests after correcting for incompleteness. The average value of  $V/V_{\text{max}}$ ,  $\langle V/V_{\text{max}} \rangle$ , for the entire sample at 9  $\mu\text{m}$  is  $0.41 \pm 0.02$  (before completeness correction) and  $0.47 \pm 0.02$  (after completeness correction). Similarly for 18  $\mu\text{m}$ ,  $\langle V/V_{\text{max}} \rangle$  is  $0.46 \pm 0.02$  (before completeness correction) and  $0.51 \pm 0.02$  (after completeness correction). In this study, we basically assume that our samples do not show any evolution (i.e, the spatial distribution of samples does not change with redshift), because they are located in the nearby ( $z \sim 0.04$ ) universe. Therefore, these results indicate that completeness correction works satisfactorily.

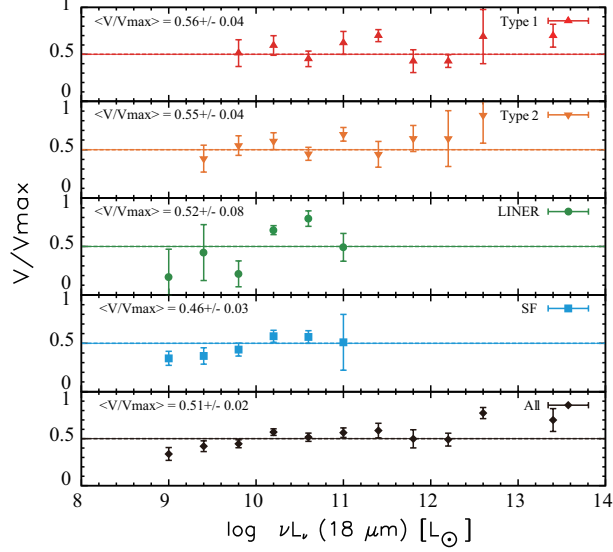


**Fig. 11.** Average values of  $V/V_{\max}$  for the different types of galaxies as a function of  $18 \mu\text{m}$  luminosity.

### 3. The Luminosity Functions at 9 and $18 \mu\text{m}$

#### 3.1. The Luminosity Function of Mid-Infrared Galaxies

Here we obtain the LFs (i.e., the volume density of galaxies per unit magnitude range) of our AKARI MIR galaxies. The LFs are derived by following the  $1/V_{\max}$  method as described by Schmidt (1968). The volume density  $\phi(L)$  and its uncertainty  $\sigma_{\phi(L)}$  are derived using the following expressions:

$$\phi(L) = \sum_i^N \frac{1}{V_{\max,i}}, \quad (10)$$

$$\sigma_{\phi(L)} = \sqrt{\sum_i^N \frac{1}{V_{\max,i}^2}}, \quad (11)$$

where  $V_{\max}$  is the maximum comoving volume of  $i$ th galaxies after applying K-correction and completeness correction, and the sum is over all galaxies in each luminosity bin.

The LFs of all galaxies at 9 and  $18 \mu\text{m}$  are given in table 3. Figure 12 shows the resulting LFs at 9 and  $18 \mu\text{m}$ . We also fit the LFs for all galaxies using the double-power law (Marshall 1987):

$$\phi(L)dL = \phi^* \left\{ \left( \frac{L}{L^*} \right)^{-\alpha} + \left( \frac{L}{L^*} \right)^{-\beta} \right\}^{-1} \frac{dL}{L^*}. \quad (12)$$

The free parameters are the characteristic luminosity  $L^*$ , the normalization factor  $\phi^*$ , the faint end slope  $\alpha$ , and the bright end slope  $\beta$ , respectively. The best-fitting values are summarized in table 4. As shown in table 4, the shapes of the 9 and  $18 \mu\text{m}$  LFs are consistent with each other.

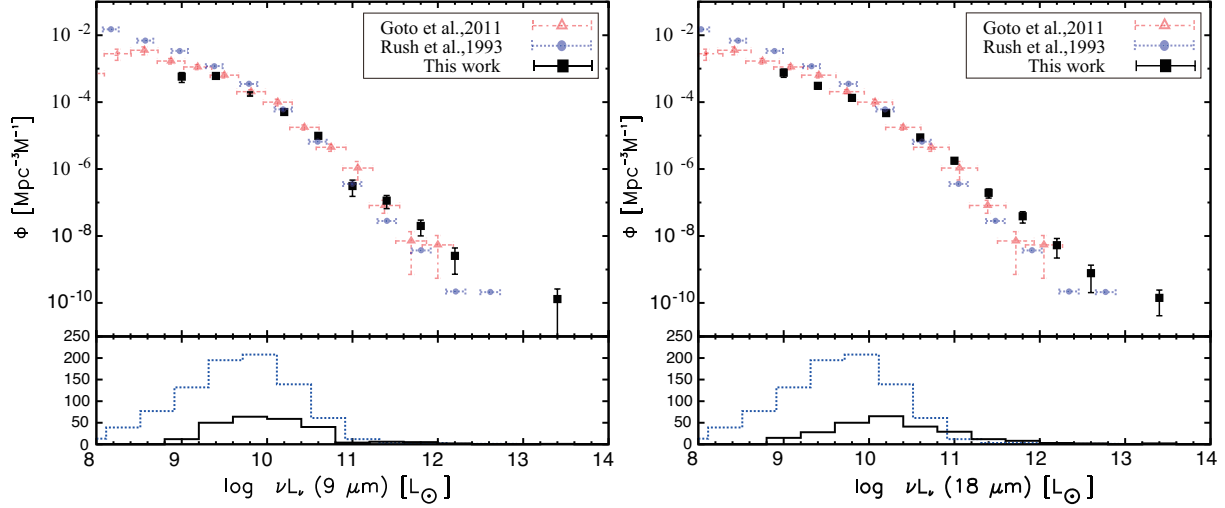


**Fig. 12.** LFs at 9 (left) and 18 (right)  $\mu\text{m}$  for all galaxies, plotted in terms of volume density as a function of luminosity. The 12  $\mu\text{m}$  LFs from Rush, Malkan, & Spinoglio (1993) after converting  $\nu L_\nu(12\mu\text{m})$  to  $\nu L_\nu(9, 18\mu\text{m})$  and the TIR LFs (Goto et al. 2011) after converting  $\nu L_{TIR}$  to  $\nu L_\nu(9, 18\mu\text{m})$  are also plotted for comparison. The vertical error bars are calculated from the Poisson statistical uncertainty and the horizontal error bars represent the uncertainty of conversion to  $\nu L_\nu(9, 18\mu\text{m})$ .

In figure 12, the 12  $\mu\text{m}$  LFs of Rush, Malkan, & Spinoglio (1993) and the 9 and 18  $\mu\text{m}$  LFs of Goto et al. (2011) are also plotted for comparison, after the conversion of their wavelength to ours. Goto et al. (2011) constructed the total infrared (TIR) LFs using AKARI's six IR bands and reported the relation between  $L_{TIR}$  and  $\nu L_\nu(9, 18\mu\text{m})$ . Therefore, we converted  $L_{TIR}$  into  $\nu L_\nu(9, 18\mu\text{m})$  using the following formulae:

$$\log[\nu L_\nu(9\mu\text{m})] = (1.04 \pm 0.01) \times \log(L_{TIR}) - (1.28 \pm 0.31), \quad (13)$$

$$\log[\nu L_\nu(18\mu\text{m})] = (1.10 \pm 0.01) \times \log(L_{TIR}) + (1.96 \pm 0.40), \quad (14)$$

as calculated by Goto et al. (2011, private communication). For the 12  $\mu\text{m}$  LFs, we calculated the conversion factors by plotting  $\nu L_\nu(12\mu\text{m})$  versus  $\nu L_\nu(9, 18\mu\text{m})$ , as shown in figure 13 and by Goto et al. (2011), and obtained these formulae:

$$\log[\nu L_\nu(9\mu\text{m})] = (1.010 \pm 0.007) \times \log[\nu L_\nu(12\mu\text{m})] - (0.23 \pm 0.07), \quad (15)$$

$$\log[\nu L_\nu(18\mu\text{m})] = (1.077 \pm 0.007) \times \log[\nu L_\nu(12\mu\text{m})] - (0.92 \pm 0.07). \quad (16)$$

The shapes of the LFs obtained from previous studies (Rush et al. 1993, Goto et al. 2011) are in good agreement with our determinations, within the error, except for low-luminosity populations. The cause of the differences in the low-luminosity regime is possibly the effect of local inhomogeneities (particularly the Virgo supercluster) in the IRAS survey, as suggested by many authors. For instance, Fang et al. (1998) selected a sample of 668 galaxies from the IRAS Faint Source Survey and derived 12  $\mu\text{m}$  LFs. They compared their LFs with Rush, Malkan, &

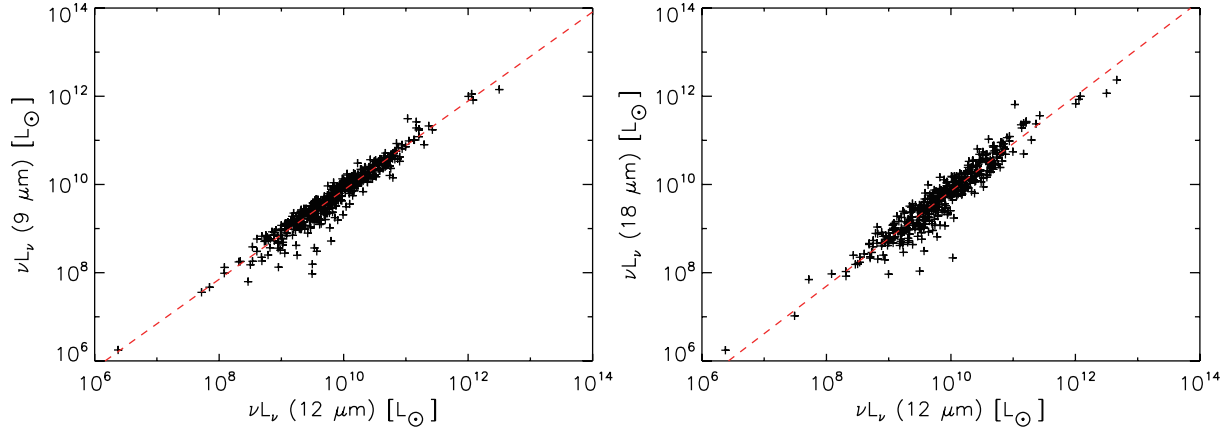


**Fig. 13.** AKARI 9  $\mu\text{m}$  versus IRAS 12  $\mu\text{m}$  luminosities (left) and AKARI 18  $\mu\text{m}$  versus IRAS 12  $\mu\text{m}$  luminosities (right). The red dotted lines show the best-fitting linear function.

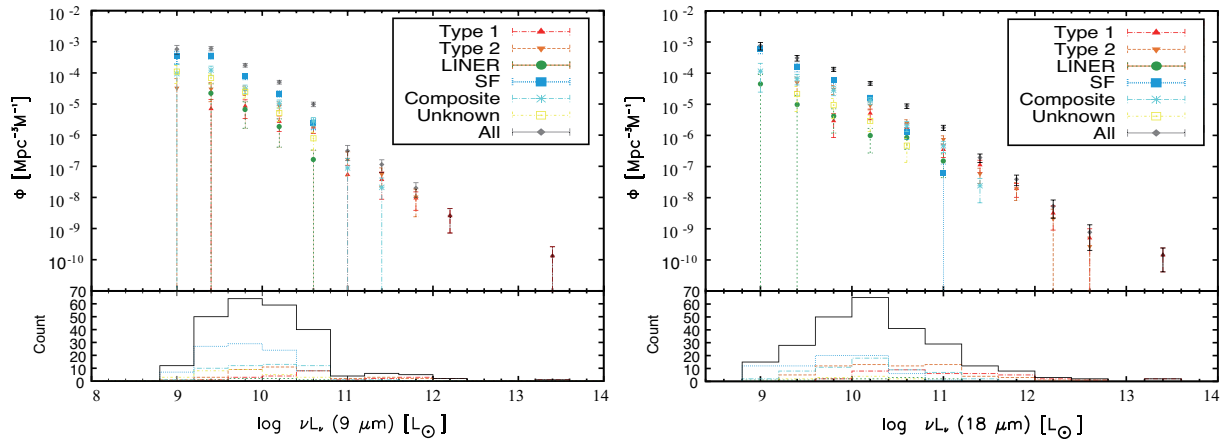


**Fig. 14.** LFs at 9 (left) and 18 (right)  $\mu\text{m}$  for each type of galaxy, plotted in terms of volume density as a function of luminosity. The error bars are calculated from the Poisson statistical uncertainty.

Spinoglio (1993) and explained the overestimates of number densities in the low-luminosity region as being introduced by the peculiar motion of the local supercluster. The threshold redshift values adopted by Rush, Malkan, & Spinoglio (1993) are  $1.0 \times 10^{-5}$  and  $4.0 \times 10^{-4}$  by Goto et al. (2011). These values are much smaller than the value adopted by us in this study (0.006). As a result, their LFs are probably affected in some way by the local supercluster.

The LFs for each spectroscopic type of galaxies at 9 and 18  $\mu\text{m}$  are given in tables 5 and 6, respectively. Figure 14 shows the LFs at 9 and 18  $\mu\text{m}$  for each type of galaxy. SFs are the most numerous objects at low luminosities, while AGNs dominate the volume density at luminosities above  $\sim 10^{11} L_{\odot}$ . Above  $\sim 10^{11} L_{\odot}$ , the volume densities of Type 1s and Type 2s are similar, except that Type 1s extend to a higher peak luminosity ( $\gtrsim 10^{12} L_{\odot}$ ). This tendency was also reported by Rush, Malkan, & Spmoglio (1993), based on their 12  $\mu\text{m}$  flux-limited sample using the IRAS Faint Source Catalog (FSC).

## 4. DISCUSSION

### 4.1. Number Density Ratio of Type 1 AGNs and Type 2 AGNs

We compare the number density of Type 1 AGNs with that of Type 2s to constrain the structure of the hypothesized torus invoked by unification. We assume that the MIR luminosity of Type 1s and Type 2s should be intrinsically the same. In this study, we use  $18\ \mu\text{m}$  luminosity, which is expected to be direct radiation from the dust torus, uninfluenced by dust extinction (the  $9\ \mu\text{m}$  flux, in contrast, may be more affected by silicate absorption or emission). By integrating the LFs of Type 1s and Type 2s separately, we obtain the number density ratio,  $\Phi_{\text{Type2}}/\Phi_{\text{Type1}}$ . Here the number density  $\Phi$  is given by the formula

$$\Phi = \int_L \phi(L)dL \sim \sum_i \phi_i(L)\Delta L, \quad (17)$$

where the integral range is  $\log(\nu L_\nu) > 10^{10} L_\odot$  for both AGN types. The resulting number density ratio of Type 2s to Type 1s,  $\Phi_{\text{Type2}}/\Phi_{\text{Type1}}$ , is  $1.73 \pm 0.36$ . We then compared this value with previous results obtained from optical LFs (Hao et al. 2005b), IR LFs (Rush et al. 1993), and hard X-ray LFs (Burlon et al. 2011). Note that before comparing these results with ours, we converted each  $L_\nu$  into  $\nu L_\nu(18\ \mu\text{m})$  using the SED template (Shang et al. 2011) as follows:

$$\log(L_{[\text{OIII}]}) = \log[\nu L_\nu(18\ \mu\text{m})] - 2.47, \quad (18)$$

$$\log[\nu L_\nu(12\ \mu\text{m})] = \log[\nu L_\nu(18\ \mu\text{m})] - 0.04, \quad (19)$$

$$\log(L_{15\text{keV}}) = \log[\nu L_\nu(18\ \mu\text{m})] - 0.61. \quad (20)$$

Table 7 shows the results of the comparison after applying this luminosity conversion.

First, we compare our result with that of Hao et al. (2005b). Hao et al. (2005b) selected 3,000 AGNs using the SDSS redshift range of  $0 \leq z \leq 0.15$  and presented the emission line LFs for Type 1s and Type 2s. In this study, we focus on the luminosity of the [OIII] line as a tracer of AGN activity. [OIII] can be excited by not only an AGN but also by massive stars in star-forming galaxies. However, such galaxies cannot contaminate the AGN samples, because the BPT line ratio classification will exclude star-forming galaxies from our AGN sample because of their [NII]/H $\alpha$  ratios. The Type 2/Type 1 ratio obtained from the [OIII] LF in Hao et al. (2005b) is  $\sim 0.67$ , which is smaller than our result (see table 7). This difference may indicate that Hao et al. systematically underestimated the intrinsic [OIII] luminosities of Type 2s. This situation may be occurred when the [OIII] emission from NLR of Type 2s are partially blocked by the dust torus. However, above explanation would contradict the basic premise of simple unification that is expected the intrinsic differences do not exist between Type 1 and Type 2 AGNs.

Next, we compared our result with Rush, Malkan, & Spinoglio (1993) and Burlon et al. (2011). As mentioned in section 3, Rush, Malkan, & Spinoglio (1993) constructed  $12\ \mu\text{m}$  LFs

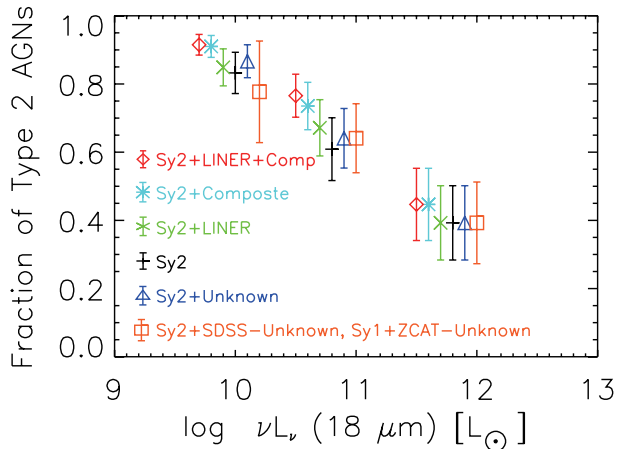


**Fig. 15.** Fraction of Type 2 AGNs to the all AGNs versus  $18 \mu\text{m}$  luminosity at  $0.006 \leq z \leq 0.2$ . Each symbol represents which populations were included with Type 2 or Type 1s. We basically considered only Sy2s to be Type 2s (black plus). However, we also estimated the fraction when we considered Sy2 + LINERs + Composites (red diamond), Sy2 + Composites (aqua asterisk), Sy2 + LINERs (green cross), and Sy2 + Unknown (blue triangle) as Type 2s. Furthermore, we also estimated the fraction under the assumption that the Unknown-SDSS galaxies are Type 2s and the Unknown ZCAT galaxies are Type 1s (orange square). Each symbol except for black plus (Sy2) was moved aside to avoid complexity.

for Type 1 and Type 2s using the IRAS FSC. Burlon et al. (2011) also constructed AGN samples in the local universe ( $z \leq 0.1$ ) using data from the Swift-BAT telescope and calculated the X-ray (15-55 keV) LFs of absorbed and unabsorbed AGNs, which were classified according to their absorbing column density ( $N_H$ ). The results obtained from the  $12 \mu\text{m}$  and hard X-ray LFs are  $\sim 1.75$  and  $\sim 1.63$ , respectively, as shown in table 7, which is in good agreement with our results. This indicates that there are a large number of narrow-line AGNs in the local universe. This is also consistent with previous conclusions from X-ray observations (Maiolino et al. 1998; Risaliti et al. 1999; Malizia et al. 2009). Note that the classification by X-ray (unabsorbed and absorbed AGNs) does not necessarily correspond to optical classifications (Type 1 and Type 2s). Some absorbed AGN samples in Burlon et al. (2011) tended to be classified as Type 1s by optical observations. This tendency indicates that the number density ratio  $\Phi_{\text{Type2}}/\Phi_{\text{Type1}}$  obtained from X-ray classification would be slightly larger than that from optical classification, which is further consistent with our estimate.

#### 4.2. Implication for the Covering Factor of the Dust Torus

Figure 15 shows the fraction of Type 2 AGNs as a function of  $18 \mu\text{m}$  luminosity. It is a decreasing function. Note that the redshift range of the Type 2s plotted in figure 15 is limited to  $0.006 \leq z \leq 0.2$ , because the SDSS spectroscopic catalog may not be as complete for Type 2s at  $z \geq 0.2$  compared with Type 1s. Before interpreting this result, we should consider the effect of (i) our classification of Type 2, (ii) unknown types of galaxies, (iii) our “rejected” galaxies, and (iv) the detection limit of the  $\text{H}\alpha$  line for the SDSS spectroscopic survey.



#### 4.2.1. Effect of Type 2 AGN classification

In this study, we basically only considered Seyfert 2 galaxies to be Type 2s. However, most of the LINERs seem to also follow the distribution of Type 2s. Moreover, some of the Composites can harbor low-luminosity Type 2s. Hence, we examined the effect these populations might have if they were included in the fraction of Type 2s. For this, we made four possible groups of Type 2s.

1. Seyfert 2 galaxies (Sy2s)
2. Sy2s + LINERs
3. Sy2s + Composites
4. Sy2s + LINERs + Composites

Figure 15 also shows the fraction of the Type 2s when LINERs and/or Composites were added to the Type 2 category as described above. As shown in this figure, the fraction of Type 2s decreases with 18  $\mu\text{m}$  luminosity regardless of the changes in the Type 2 classification criteria.

#### 4.2.2. Effect of Unknown types of galaxies

As we described in section 2.2, 11 galaxies were classified as Unknown types of galaxies for the 18  $\mu\text{m}$  sample. The redshift range of these galaxies is less than 0.2. Among the 11 galaxies, 6 were obtained from the SDSS, and 5 were obtained from the ZCAT. We found that none of these SDSS galaxies were Type 1s (see section 2.2). On the other hand, we could not constrain the 5 ZCAT galaxies, because the ZCAT does not include spectroscopic line information. Therefore, we considered the effect of these objects by including two extreme possibilities as follows:

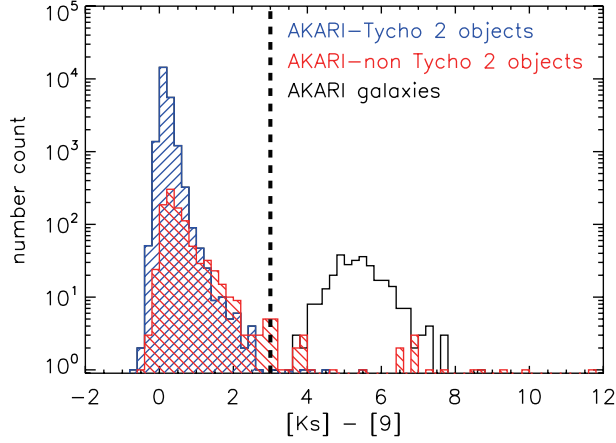
- 6 SDSS galaxies and 5 ZCAT galaxies are Type 2s.
- 6 SDSS galaxies are Type 2s and 5 ZCAT galaxies are Type 1s.

Figure 15 also shows the fractions of Type 2s considering both of these cases. As shown in this figure, the fraction of Type 2s still decreases with 18  $\mu\text{m}$  luminosity regardless of the classification of the Unknown objects.

#### 4.2.3. Effect of rejected galaxies

In section 2.1, we selected 243 and 255 galaxies at 9 and 18  $\mu\text{m}$ , respectively. However, it should be noted that when we cross-matched the AKARI-ZCAT objects, 1,331 AKARI sources did not match within 12 arcsec; thus, we rejected these objects for this study. If these objects were galaxies, our results would be affected. For an estimate of their effect, these 1,331 objects (hereinafter AKARI-non-Tycho 2 objects) were cross-matched with the 2MASS Point Source Catalog (Skrutskie et al. 2006) to investigate their color distributions. We adopted 3 arcsec as our search radius, which was optimized for cross-identification between these two catalogs (Ishihara et al. 2010).

Figures 16 and 17 show the histogram of [Ks]-[9] and [9]-[18] for AKARI-non-Tycho 2 objects. Here [Ks], [9], and [18] represent Vega magnitudes in the 2MASS Ks (2.2  $\mu\text{m}$ ), AKARI



**Fig. 16.** Color ( $[Ks] - [9]$ ) distribution of AKARI sources. The blue line represents the AKARI-Tycho 2 objects, the red line represents the AKARI-non-Tycho 2 objects, and the black line represents the AKARI galaxies. The dotted line indicates the threshold between stars and galaxies. We extracted the AKARI-non Tycho 2 objects with  $[Ks] - [9] \geq 3$  as galaxy candidates.

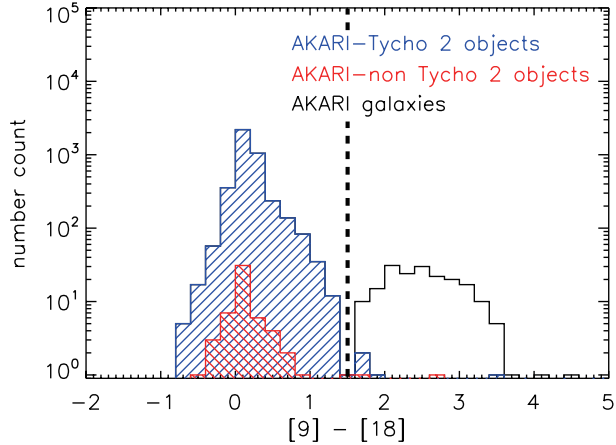


**Fig. 17.** Color ( $[9] - [18]$ ) distribution of AKARI sources. The blue line represents the AKARI-Tycho 2 objects, the red line represents the AKARI-non-Tycho 2 objects, and black line represents the AKARI galaxies. The dotted line indicates the threshold between stars and galaxies. We extracted the AKARI-non-Tycho 2 objects with  $[9] - [18] \geq 1.5$  as galaxy candidates.

$9 \mu\text{m}$ , and AKARI  $18 \mu\text{m}$  bands, respectively. The zero point magnitudes for the  $9$  and  $18 \mu\text{m}$  bands are  $56.3$  and  $12.0$  Jy, respectively (Tanabé et al. 2008). To ensure the reliability of the color diagram, the AKARI-Tycho 2 sources and our samples in this study (AKARI galaxies) were also plotted in these figures. As shown in the figures, the AKARI-Tycho 2 stars were well-separated from the AKARI galaxies. Thus, color distribution distinguishes stars from galaxies. In this study, we extracted galaxy candidates using these two colors. We first extracted 27 AKARI-non-Tycho 2 objects that met the following criterion as galaxy candidates:

$$[Ks] - [9] \geq 3.0. \tag{21}$$

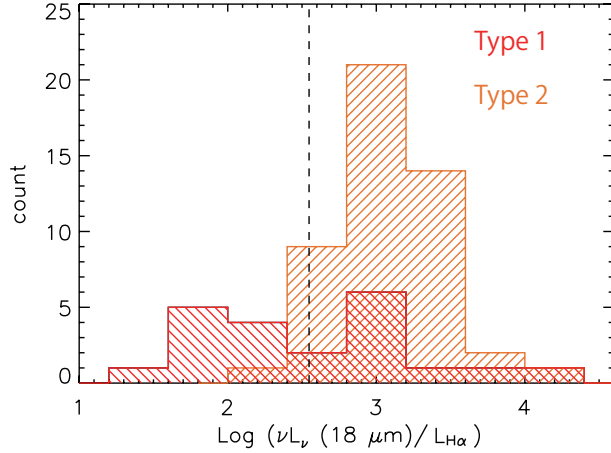


**Fig. 18.** Distribution of  $\nu L_{\nu}(18\mu\text{m})/L_{H\alpha}$ . The dashed line represents the average value of the above ratio.

323 AKARI-non-Tycho 2 objects could not be classified as a star or galaxy. These objects are missing one or both of [Ks] and [9] data; thus, we could not investigate their [Ks] - [9] color. For these 323 objects, we examined the [9]-[18] color distribution (figure 17) and extracted 2 objects that met the following criterion as galaxy candidates:

$$[9] - [18] \geq 1.5. \quad (22)$$

Also, 265 AKARI-non-Tycho 2 objects could not be identified as a star or galaxy, because they did not have one or both of [9] or [18] data; thus, we could not investigate their [9]-[18] color. As a result,  $27 + 2 + 265 = 294$  objects (278 objects for  $9\mu\text{m}$  and 31 objects for  $18\mu\text{m}$ ) remained as galaxy candidates. For these objects, we carefully determined their type using the previous literature. Finally, 276 objects were confirmed as stars or planetary nebulae, thus,  $294 - 276 = 18$  objects remained as galaxies (13 objects for  $9\mu\text{m}$  and 7 objects for  $18\mu\text{m}$ ). The maximum uncertainty caused by including them as galaxies would be  $13/243 \sim 0.053$  (5.3%) for the  $9\mu\text{m}$  sample and  $7/255 \sim 0.027$  (2.7%) for the  $18\mu\text{m}$  sample, respectively.

#### 4.2.4. Effect of the detection limit of the $H\alpha$ line for the SDSS spectroscopic survey

Finally, we consider the SDSS detection limit for the detection of the broad  $H\alpha$  line from the Type 1s in the lowest luminosity bin. If the detection limit was not sufficiently low to detect some Type 1s, the fraction of Type 2s could be overestimated, especially in the lowest luminosity bin in figure 15. To investigate this, we estimated the detection limit of the  $H\alpha$  line, considering the typical luminosity ratio between  $H\alpha$  and  $18\mu\text{m}$  of Type 1s. Figure 18 shows the distribution of luminosity ratio of the  $18\mu\text{m}$  luminosity to the  $H\alpha$  luminosity for the AKARI-SDSS AGNs.

In this study, we adopted  $\log[\nu L_{\nu}(18\mu\text{m})/L_{H\alpha}] \sim 2.55$  as the typical luminosity ratio between the  $H\alpha$  and  $18\mu\text{m}$  of Type 1s. Next, we investigated all AGNs in the SDSS DR7 spectroscopic region. According to the FWHM of  $H\alpha$  and the BPT diagram, 26,568 AGNs

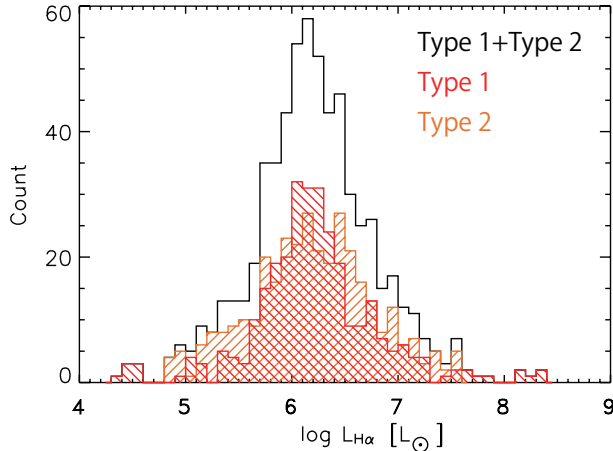


**Fig. 19.** Distribution of  $L_{H\alpha}$  for all SDSS AGNs ( $0.006 \leq z \leq 0.03$ ).

were then extracted. Furthermore, we extracted 652 AGNs with a redshift between 0.006 and 0.03 focusing on the lowest luminosity bin ( $\sim 10^{10} L_{\odot}$ ) in figure 15, which corresponds to  $z \sim 0.03$  (see figure 8).

Figure 19 shows the distribution of  $L_{H\alpha}$  for the 652 AGNs. As shown in figure 19, these histograms go down to the faintest bin of  $L_{H\alpha} \sim 10^5 L_{\odot}$ , which is consistent with the histogram of  $L_{H\alpha}$  obtained by (Hao et al. 2005b). This limit corresponds to  $\sim 10^{7-8} L_{\odot}$  for our  $18 \mu\text{m}$  AGNs, assuming the typical luminosity ratio. Therefore, the detection limit seems sufficiently low to detect the broad  $H\alpha$  lines from the Type 1s in the lowest luminosity bin ( $\sim 10^{10} L_{\odot}$ ) even if we adopted the maximum value ( $\sim 4$ ) of  $\nu L_{\nu}(18 \mu\text{m})/L_{H\alpha}$  distribution as the typical luminosity ratio.

The decreasing fraction of Type 2s at increasing luminosity could mean that the luminosity from the central engine influences the structure of the torus. The covering factor of the dust torus is smaller for more luminous AGNs, possibly because increasing luminosity sublimates more dust, causing the inner radius of the dust torus to recede (Lawrence 1991). This result has been reported several times in the past. For example, Maiolino et al. (2007) found that the MIR spectra of 25 AGNs taken with IRS on board the Spitzer Space Telescope showed a negative correlation between  $\nu L_{6.7}/\nu L_{5100}$  and the  $[\text{OIII}]\lambda 5007$  line luminosity.  $L_{6.7}$  and  $L_{5100}$  are the continuum luminosity at the rest-frame wavelength of  $6.7 \mu\text{m}$  and  $5100 \text{ \AA}$ , respectively. They mentioned that one possible explanation was that higher  $[\text{OIII}]$  luminosities imply a more luminous central engine and larger dust sublimation radius, suggesting that a larger dust sublimation radius would give a lower covering factor of dust if the obscuring medium is distributed in a disk with constant height. Recently, Burlon et al. (2011) reported a negative correlation between the fraction of absorbed AGN and hard X-ray luminosity using a Swift-BAT sample. Our study confirms and extends these results with AKARI, by taking our larger MIR sample. We emphasize that a luminosity-dependent torus geometry destroys

the simplicity of the original torus unification scheme, and now requires that at least one new free function must be determined. The torus covering fraction as a function of AGN luminosity can be measured from complete MIR observations, with our figure 15 as a first effort to do so.

## 5. SUMMARY

Using the AKARI MIR all-sky survey, we constructed the 9 and 18  $\mu\text{m}$  LFs for all types of local galaxies. Using nearly complete optical spectroscopy of emission lines, we made a classification based on the width of  $\text{H}\alpha$  or the emission line ratios of  $[\text{OIII}]/\text{H}\beta$  and  $[\text{NII}]/\text{H}\alpha$ . We classified the AKARI sources into five types (Type 1 AGNs, Type 2 AGNs, LINERs, Composites, and SFs). We then calculated the number density of Type 1 AGNs and Type 2 AGNs by integrating each LF. The main results are as follows:

1. AKARI's efficiency at identifying AGNs is excellent, with 41% of our 18  $\mu\text{m}$  sources hosting active nuclei.
2. The number density ratio of Type 2 to Type 1 AGNs obtained from the 18  $\mu\text{m}$  LF is  $1.73 \pm 0.36$ . That value is larger than the results obtained from the optical ( $[\text{OIII}]$ ) LF (Hao et al. 2005b). The cause of this difference is probably the absorption of the  $[\text{OIII}]$  photons by the dust torus in Type 2 AGNs in particular. On the other hand, the results obtained from the MIR (12  $\mu\text{m}$ ) and hard X-ray (15-55 keV) LFs are consistent with each other.
3. The fraction of Type 2s among all AGNs decreases with increasing 18  $\mu\text{m}$  luminosity. Thus, the covering factor of the dust torus probably depends on the 18  $\mu\text{m}$  luminosity. Our MIR results are also comparable to those reported using optical and X-ray observations.

These results suggest that most of the AGNs in the local universe are obscured, but the obscuration (whether by a torus or another mechanism) decreases with MIR luminosity. Furthermore, these obscured AGNs are well-measured using MIR surveys, just as they are by complementary hard X-ray surveys.

Recently, the Wide-field Infrared Survey Explorer (WISE; Wright et al. 2010) all-sky survey data was released. WISE has performed a digital imaging survey of the entire sky in the 3.4, 4.6, 12, and 22  $\mu\text{m}$  MIR bandpasses. This has been used to construct AGN samples extending to substantial redshifts (e.g., Edelson & Malkan 2012). The present study with AKARI provides us with an important local benchmark for AGN studies at high redshift.

This study is based on observations made with AKARI. AKARI is a JAXA project with the participation of ESA. The authors gratefully acknowledge the anonymous referee for a careful reading of the manuscript and very helpful comments. We also thank P.Gandhi (Durham University) and T.Goto (University of Copenhagen) for fruitful discussion. Funding for the SDSS and SDSS-II has been provided by the Alfred P. Sloan Foundation, the Participating Institutions, the National Science Foundation, the U.S. Department of Energy, the National Aeronautics and Space Administration, the Japanese Monbukagakusho, the Max Planck

Society, and the Higher Education Funding Council for England. The SDSS Web Site is <http://www.sdss.org/>. The SDSS is managed by the Astrophysical Research Consortium for the Participating Institutions. The Participating Institutions are the American Museum of Natural History, Astrophysical Institute Potsdam, University of Basel, University of Cambridge, Case Western Reserve University, University of Chicago, Drexel University, Fermilab, the Institute for Advanced Study, the Japan Participation Group, Johns Hopkins University, the Joint Institute for Nuclear Astrophysics, the Kavli Institute for Particle Astrophysics and Cosmology, the Korean Scientist Group, the Chinese Academy of Sciences (LAMOST), Los Alamos National Laboratory, the Max-Planck-Institute for Astronomy (MPIA), the Max-Planck-Institute for Astrophysics (MPA), New Mexico State University, Ohio State University, University of Pittsburgh, University of Portsmouth, Princeton University, the United States Naval Observatory, and the University of Washington. This research is also made use of the NASA/IPAC Extragalactic Database (NED) which is operated by the Jet Propulsion Laboratory, California Institute of Technology, under contract with the National Aeronautics and Space Administration. This research has also made use of the SIMBAD database, operated at CDS, Strasbourg, France.

## References

- Abazajian, K. N., et al. 2009, *ApJS*, 182, 543  
Alonso-Herrero, A., et al. 2011, *ApJ*, 736, 82  
Alonso-Herrero, A., Pereira-Santaella, M., Rieke, G. H., & Rigopoulou, D. 2012, *ApJ*, 744, 2  
Antonucci, R. 1993, *ARA&A*, 31, 473  
Baldwin, J. A., Phillips, M. M., & Terlevich, R. 1981, *PASP*, 93, 5  
Beichman, C. A., Neugebauer, G., Habing, H. J., Clegg, P. E., & Chester, T. J. 1988, *Infrared Astronomical Satellite (IRAS) Catalogs and Atlases, Vol. 1, Explanatory Supplement* (Washington, D.C.: GPO)  
Bukhmastova, Y. L. 2001, *Astronomy Reports*, 45, 581  
Burlon, D., Ajello, M., Greiner, J., Comastri, A., Merloni, A., & Gehrels, N. 2011, *ApJ*, 728, 58  
Caccianiga, A., Maccacaro, T., Wolter, A., Della Ceca, R., & Gioia, I. M. 2000, *A&AS*, 144, 247  
Clavel, J., et al. 2000, *A&A*, 357, 839  
Cohen, M. 1992, *AJ*, 103, 1734  
Corbett, E. A., et al. 2003, *ApJ*, 583, 670  
Edelson, R., & Malkan, M. 2012, *ApJ*, 751, 52  
Eisenstein, D. J., et al. 2001, *AJ*, 122, 2267  
Fang, F., Shupe, D. L., Xu, C., & Hacking, P. B. 1998, *AJ*, 500, 693  
Goto, T., et al. 2011, *MNRAS*, 410, 573  
Hao, L., et al. 2005, *AJ*, 129, 1783  
Hao, L., et al. 2005, *AJ*, 129, 1795  
Ho, L. C., Filippenko, A. V., & Sargent, W. L. W. 1997, *ApJS*, 112, 315

Høg, E., et al. 2000, *A&A*, 355, L27  
Huchra, J. P., Geller, M. J., & Corwin, H. G., Jr. 1995, *ApJS*, 99, 391  
Ishihara, D., et al. 2010, *A&A*, 514, 1  
Ishihara, D., Kaneda, H., Onaka, T., Ita, Y., Matsuura, M., & Matsunaga, N. 2011, *A&A*, 534, 79  
Kataza et al. 2010, AKARI-IRC Point Source Catalogue Release note Version 1.0  
Kauffmann, G., et al. 2003, *MNRAS*, 346, 1055  
Kewley, L. J., Heisler, C. A., Dopita, M. A., & Lumsden, S. 2001, *ApJS*, 132, 37  
Kewley, L. J., Groves, B., Kauffmann, G., & Heckman, T. 2006, *MNRAS*, 372, 961  
Kirhakos, S. D., & Steiner, J. E. 1990, *AJ*, 99, 1722  
Konstantopoulos, I. S., et al. 2012, *ApJ*, 745, 30  
Koulouridis, E., Chavushyan, V., Plionis, M., Krongold, Y., & Dultzin-Hacyan, D. 2006, *ApJ*, 651, 93  
Lawrence, A. 1991, *MNRAS*, 252, 586  
Leech, K. J., Penston, M. V., Terlevich, R., Lawrence, A., Rowan-Robinson, M., & Crawford, J. 1989, *MNRAS*, 240, 349  
Maiolino, R., Salvati, M., Bassani, L., Dadina, M., della Ceca, R., Matt, G., Risaliti, G., & Zamorani, G. 1998, *A&A*, 338, 781  
Maiolino, R., Shemmer, O., Imanishi, M., Netzer, H., Oliva, E., Lutz, D., & Sturm, E. 2007, *A&A*, 468, 979  
Malizia, A., Stephen, J. B., Bassani, L., Bird, A. J., Panessa, F., & Ubertini, P. 2009, *MNRAS*, 399, 944  
Marshall, H. L. 1987, *AJ*, 94, 628  
Mor, R., Netzer, H., & Elitzur, M. 2009, *ApJ*, 705, 298  
Moustakas, J., & Kennicutt, R. C., Jr. 2006, *ApJS*, 164, 81  
Murakami, H., et al. 2007, *PASJ*, 59, 369  
Nenkova, M., Sirocky, M. M., Ivezić, Ž., & Elitzur, M. 2008, *ApJ*, 685, 147  
Nenkova, M., Sirocky, M. M., Nikutta, R., Ivezić, Ž., & Elitzur, M. 2008, *ApJ*, 685, 160  
Neugebauer, G., et al. 1984, *Astrophys. Lett.*, 278, L1  
Parra, R., Conway, J. E., Aalto, S., Appleton, P. N., Norris, R. P., Pihlström, Y. M., & Kewley, L. J. 2010, *ApJ*, 720, 555  
Petrosian, V. 1976, *Astrophys. Lett.*, 209, L1  
Petrosian, A., McLean, B., Allen, R. J., & MacKenty, J. W. 2007, *ApJS*, 170, 33  
Petrosian, A., McLean, B., Allen, R., Kunth, D., & Leitherer, C. 2008, *ApJS*, 175, 86  
Poggianti, B. M., & Wu, H. 2000, *ApJ*, 529, 157  
Richards, G. T., et al. 2002, *AJ*, 123, 2945  
Risaliti, G., Maiolino, R., & Salvati, M. 1999, *ApJ*, 522, 157  
Rush, B., Malkan, M. A., & Spinoglio, L. 1993, *ApJS*, 89, 1  
Schmidt, M. 1968, *ApJ*, 151, 393  
Shang, Z., et al. 2011, *ApJS*, 196, 2  
Skrutskie, M. F., et al. 2006, *AJ*, 131, 1163  
Spinoglio, L., & Malkan, M. A. 1989, *ApJ*, 342, 83  
Strauss, M. A., et al. 2002, *AJ*, 124, 1810

Tanabé, T., et al. 2008, PASJ, 60, 375  
Urry, C. M., & Padovani, P. 1995, PASP, 107, 803  
Veilleux, S., & Osterbrock, D. E. 1987, ApJS, 63, 295  
Veilleux, S., Kim, D.-C., Sanders, D. B., Mazzarella, J. M., & Soifer, B. T. 1995, ApJS, 98, 171  
Veron-Cetty, M.-P., & Veron, P. 1986, A&AS, 66, 335  
Wang, L., & Rowan-Robinson, M. 2009, MNRAS, 398, 109  
Werner, M. W., et al. 2004, ApJS, 154, 1  
Wright, E. L., et al. 2010, AJ, 140, 1868  
Wu, H., Zou, Z. L., Xia, X. Y., & Deng, Z. G. 1998, A&AS, 132, 181  
Yamamura, I., Makiuti, S., Ikeda, N., Fukuda, Y., Oyabu, S., Koga, T., & White, G. J. 2010, VizieR  
Online Data Catalog, 2298, 0  
Yamauchi, C., et al. 2011, PASP, 123, 852  
Yamauchi, C. 2011, PASP, 123, 1324  
Yuan, T.-T., Kewley, L. J., & Sanders, D. B. 2010, ApJ, 709, 884



**Table 1.** List of 348 galaxies.

name	RA j2000	DEC j2000	$f_{9\mu m}$ (Jy)	$f_{18\mu m}$ (Jy)	z	type	ref
2MASX J00090793+1427558	00:09:07.90	+14:27:56.7	0.052	0.248	0.041	Type 2	(1)
ARP 256 (3)01	00:18:50.92	-10:22:37.4	0.178	0.517	0.027	Composite	(1)
NGC 0192	00:39:13.39	+00:51:49.4	0.185	—	0.014	SF	(4)
NGC 0291	00:53:29.91	-08:46:02.9	—	0.204	0.019	Type 2	(1)
UGC 00774	01:13:50.91	+13:16:19.2	0.123	0.324	0.050	Type 1	(2),(3)
CGCG 436-030	01:20:02.61	+14:21:42.4	0.182	0.592	0.031	Composite	(1)
2MASX J01221811+0100262	01:22:17.93	+01:00:26.1	—	0.306	0.055	SF	(1)
MRK 0995	01:27:29.21	-08:33:14.0	0.132	0.150	0.049	Composite	(1)
GIN 086	01:37:06.98	-09:08:57.7	—	0.197	0.070	Type 2	(1)
UGC 01260	01:48:33.18	+12:36:50.1	0.141	0.214	0.018	SF	(3)
SDSS J015103.75-094209.8	01:51:03.66	-09:42:12.1	0.259	0.348	0.006	SF	(6)
NGC 0716	01:52:59.63	+12:42:30.8	0.262	0.342	0.015	LINER	(7)
MRK 1014	01:59:50.31	+00:23:39.7	—	0.244	0.163	Type 1	(1)
NGC 0835	02:09:24.61	-10:08:09.5	0.247	0.342	0.014	Type 2	(2),(3)
IC 0210	02:09:28.24	-09:40:46.9	0.185	—	0.006	Unknown	—
NGC 0838	02:09:38.53	-10:08:47.0	0.514	0.861	0.013	SF	(1)
NGC 0839	02:09:42.76	-10:11:02.5	0.297	1.101	0.013	SF	(8)
NGC 0863	02:14:33.53	-00:46:00.8	—	0.266	0.026	Type 1	(2),(3)
NGC 0905	02:22:43.69	-08:43:10.6	—	0.188	0.046	Unknown	—
MRK 1044	02:30:05.57	-08:59:53.4	0.110	—	0.016	Type 1	(3)
UGC 02024	02:33:01.26	+00:25:15.2	0.160	0.456	0.022	Type 2	(1)
SDSS J023437.83-084716.0	02:34:37.77	-08:47:16.7	0.165	0.368	0.043	Type 1	(2)
NGC 1142	02:55:12.06	-00:11:02.8	0.265	0.380	0.029	Type 2	(2),(3)
UGC 02403	02:55:57.28	+00:41:31.4	0.205	0.392	0.014	SF	(1)
NGC 1194	03:03:49.08	-01:06:12.6	0.169	0.415	0.014	Type 2	(1)
MRK 0609	03:25:25.38	-06:08:38.8	0.125	—	0.034	Type 2	(1)
2MASX J03474022+0105143	03:47:40.15	+01:05:13.8	0.166	0.407	0.031	Type 1	(2),(3)
UGC 03973	07:42:32.81	+49:48:35.1	0.276	0.611	0.022	Type 1	(1)
MCG +05-19-001 NED02	07:44:09.11	+29:14:51.0	0.160	0.275	0.016	Type 2	(2)
NGC 2445 [ASR92] A	07:46:55.02	+39:00:54.5	0.102	0.223	0.013	SF	(3)
UGC 04132	07:59:12.92	+32:54:49.5	0.242	—	0.017	SF	(1)
NGC 2498	07:59:38.76	+24:58:56.6	—	0.346	0.016	Unknown	—
UGC 04145	07:59:40.13	+15:23:12.4	0.174	0.577	0.016	Type 2	(1)
SBS 0755+509	07:59:40.87	+50:50:24.3	—	0.178	0.055	Type 2	(1)
CGCG 118-036	07:59:53.45	+23:23:23.8	0.105	—	0.029	Type 2	(1)
SBS 0756+553	08:00:33.52	+55:13:00.2	—	0.217	0.035	Composite	(1)
2MASX J08025293+2552551	08:02:52.96	+25:52:55.0	—	0.326	0.081	Type 2	(1)

Table 1. (Continued.)

name	RA	DEC	$f_{9\mu m}$	$f_{18\mu m}$	$z$	type	ref
	j2000	j2000	(Jy)	(Jy)			
NGC 2512	08:03:08.01	+23:23:31.2	0.156	0.361	0.016	SF	(3)
MRK 1212	08:07:05.48	+27:07:33.4	—	0.213	0.041	Composite	(1)
IC 2227	08:07:07.14	+36:14:00.4	0.228	0.224	0.032	Type 2	(1)
UGC 04229	08:07:41.07	+39:00:14.8	—	0.209	0.023	Type 2	(1)
2MASX J08100697+1838176	08:10:07.00	+18:38:17.5	—	0.418	0.016	Composite	(1)
NGC 2538	08:11:23.15	+03:37:59.0	0.104	—	0.013	SF	(4)
CGCG 031-072	08:14:25.33	+04:20:32.7	0.131	—	0.033	Type 1	(9)
UGC 04306	08:17:36.68	+35:26:44.9	0.178	0.240	0.008	SF	(1)
NGC 2561	08:19:36.98	+04:39:26.5	0.140	—	0.014	Unknown	—
2MASX J08244333+2959238	08:24:43.31	+29:59:23.3	0.121	—	0.025	Type 2	(1)
MRK 0091	08:32:27.96	+52:36:21.8	0.143	0.307	0.017	SF	(1)
NGC 2623	08:38:24.05	+25:45:16.7	0.177	0.593	0.018	Unknown	—
FBQS J084215.2+402533	08:42:15.32	+40:25:32.7	0.138	0.272	0.055	Type 2	(1)
KUG 0842+400	08:46:03.97	+39:49:48.7	0.126	—	0.029	SF	(1)
IC 2406	08:48:04.58	+17:42:10.7	0.149	—	0.016	Composite	(1)
OJ +287:[YJI97] EXT	08:54:48.83	+20:06:30.7	—	0.206	0.306	Type 1	(3)
NGC 2718	08:58:50.32	+06:17:35.6	0.146	0.300	0.013	SF	(1)
2MASX J09002536+3903542	09:00:25.37	+39:03:53.8	0.312	0.794	0.058	Composite	(1)
UGC 04730	09:01:58.45	+60:09:05.9	0.106	—	0.011	Composite	(1)
NGC 2731	09:02:08.40	+08:18:04.8	0.181	—	0.009	SF	(10)
NGC 2738	09:04:00.38	+21:58:02.2	0.198	—	0.010	SF	(1)
NGC 2750	09:05:47.91	+25:26:14.0	0.121	0.197	0.009	SF	(11)
NGC 2761	09:07:30.78	+18:26:04.6	0.194	0.280	0.029	Composite	(1)
NGC 2764	09:08:17.47	+21:26:34.6	0.228	—	0.009	Unknown	—
NGC 2773	09:09:44.23	+07:10:25.2	0.187	0.182	0.018	SF	(1)
FIRST J091345.4+405628	09:13:45.41	+40:56:27.9	—	0.205	0.442	Type 2	(2),(3)
NGC 2782:[HK83] 04	09:14:05.09	+40:06:49.2	0.314	0.692	0.009	SF	(11)
NGC 2789	09:14:59.67	+29:43:47.9	0.125	—	0.021	Unknown	—
NGC 2785	09:15:15.38	+40:55:03.0	0.377	0.604	0.009	Type 2	(1)
UGC 04881	09:15:55.48	+44:19:53.2	—	0.182	0.040	LINER	(1)
SDSS J091722.85+415959.0	09:17:22.87	+41:59:59.3	0.572	1.380	0.006	Composite	(1)
MRK 0704	09:18:25.94	+16:18:18.8	0.256	0.469	0.029	Type 1	(2),(3)
CGCG 121-075	09:23:42.91	+22:54:30.8	0.078	0.178	0.033	Type 1	(1)
NGC 2854	09:24:03.16	+49:12:15.5	0.186	—	0.009	Unknown	—
NGC 2856	09:24:16.08	+49:14:57.2	0.239	0.466	0.009	Unknown	—
UGC 05025	09:26:03.31	+12:44:04.0	0.099	0.214	0.029	Type 1	(1)
UGC 05046	09:28:06.66	+17:11:47.2	0.119	—	0.014	SF	(1)
CGCG 181-049	09:30:11.21	+34:39:53.0	0.096	—	0.023	SF	(1)

Table 1. (Continued.)

name	RA	DEC	$f_{9\mu m}$	$f_{18\mu m}$	$z$	type	ref
	j2000	j2000	(Jy)	(Jy)			
SBS 0927+493	09:31:06.69	+49:04:47.7	—	0.228	0.034	LINER	(1)
UGC 05101	09:35:51.63	+61:21:13.4	0.135	0.457	0.039	Type 2	(1)
CGCG 239-011 NED02	09:36:37.14	+48:28:28.1	0.147	0.330	0.026	SF	(12)
CGCG 122-055	09:42:04.77	+23:41:07.2	—	0.231	0.021	Type 1	(1)
NGC 2966	09:42:11.49	+04:40:23.2	0.178	0.354	0.007	SF	(4)
2MASX J09452133+1737533	09:45:21.29	+17:37:52.8	—	0.286	0.128	Type 2	(1)
NGC 2990	09:46:17.13	+05:42:31.8	0.151	—	0.010	SF	(1)
IC 0563	09:46:20.29	+03:02:46.4	0.177	—	0.020	SF	(1)
I 564	09:46:20.87	+03:04:13.0	0.183	—	0.020	Composite	(1)
CGCG 007-035	09:47:13.53	+00:39:54.9	0.097	—	0.020	Composite	(1)
NGC 3055	09:55:17.98	+04:16:11.5	0.156	0.304	0.006	Composite	(1)
IC 2519	09:55:58.85	+34:02:10.9	0.046	0.175	0.021	SF	(1)
UGC 05376	10:00:27.03	+03:22:26.4	0.279	—	0.007	SF	(1)
NGC 3094	10:01:25.92	+15:46:11.6	0.707	1.505	0.008	LINER	(13)
SDSS J100131.21+465946.7	10:01:31.28	+46:59:46.8	—	0.221	0.086	Type 2	(1)
3C 234	10:01:49.52	+28:47:08.6	0.112	0.274	0.185	Type 2	(1)
UGC 05403	10:02:35.57	+19:10:37.6	0.140	0.266	0.007	SF	(1)
CGCG 064-055	10:05:51.15	+12:57:40.2	—	0.291	0.009	Type 2	(1)
IC 2551	10:10:40.30	+24:24:50.0	0.145	0.443	0.021	Composite	(1)
2MASX J10104337+0612013	10:10:43.30	+06:12:01.4	—	0.213	0.098	Type 1	(1)
NGC 3154	10:13:01.20	+17:02:03.4	0.254	0.393	0.022	SF	(1)
UGC 05613	10:23:32.60	+52:20:31.4	0.183	—	0.032	Composite	(1)
WAS 11	10:27:25.87	+20:26:50.7	0.130	—	0.019	Composite	(1)
MRK 0034	10:34:08.52	+60:01:51.4	—	0.291	0.051	Type 2	(1)
SDSS J103631.87+022144.0	10:36:31.91	+02:21:44.2	0.124	0.311	0.050	Composite	(1)
NGC 3306	10:37:10.23	+12:39:07.8	0.154	—	0.010	SF	(10)
IC 2598	10:39:42.34	+26:43:38.3	0.144	0.219	0.019	SF	(1)
MRK 0726	10:45:49.87	+27:37:12.7	—	0.186	0.044	Composite	(1)
NGC 3367	10:46:34.89	+13:45:00.8	0.168	0.606	0.010	Composite	(1)
MRK 0727	10:48:44.16	+26:03:13.4	—	0.240	0.026	SF	(1)
UGC 05941 NED02	10:50:21.58	+41:27:51.0	0.094	0.113	0.024	SF	(1)
2MASX J10563881+1419306	10:56:38.83	+14:19:28.9	—	0.209	0.081	Type 1	(1)
NGC 3471	10:59:09.07	+61:31:51.9	0.272	0.563	0.007	SF	(1)
2MASX J10591815+2432343	10:59:18.11	+24:32:34.3	0.131	0.452	0.043	LINER	(2)
UGC 06074	10:59:58.26	+50:54:10.6	—	0.421	0.010	Composite	(1)
2MASX J11001238+0846157	11:00:12.38	+08:46:12.1	0.133	0.408	0.100	Type 2	(1)
UGC 06100	11:01:34.18	+45:39:16.2	—	0.181	0.029	Type 2	(1)
UGC 06103	11:01:59.13	+45:13:42.1	0.133	—	0.020	Composite	(1)

Table 1. (Continued.)

name	RA j2000	DEC j2000	$f_{9\mu m}$ (Jy)	$f_{18\mu m}$ (Jy)	z	type	ref
CGCG 241-078	11:06:37.46	+46:02:19.2	—	0.193	0.025	Composite	(1)
NGC 3561A	11:11:12.95	+28:42:42.7	0.127	0.285	0.029	Composite	(1)
IC 2637	11:13:49.77	+09:35:10.7	0.149	0.155	0.029	Type 2	(1)
NGC 3583	11:14:10.89	+48:19:06.7	0.428	—	0.007	Unknown	—
B2 1111+32	11:14:38.97	+32:41:33.5	0.087	0.246	0.189	Type 1	(2),(3)
NGC 3633	11:20:26.30	+03:35:07.4	0.193	0.339	0.009	Composite	(1)
NGC 3656	11:23:38.46	+53:50:33.5	0.110	—	0.010	Composite	(1)
FIRST J112443.5+384546	11:24:43.62	+38:45:46.7	0.111	—	0.007	SF	(11)
IC 2810	11:25:44.92	+14:40:35.2	—	0.208	0.034	Composite	(1)
IC 2846	11:28:00.48	+11:09:28.3	—	0.209	0.041	LINER	(1)
ARP 299:[ZWM2003] 04	11:28:30.91	+58:33:42.7	1.668	7.138	0.010	Composite	(1)
SDSS J112833.61+583346.5	11:28:33.55	+58:33:46.2	0.882	4.616	0.010	Composite	(1)
IC 0698	11:29:03.86	+09:06:42.3	0.171	0.166	0.021	Composite	(1)
CGCG 126-075	11:31:03.70	+20:14:08.6	—	0.192	0.014	Composite	(1)
NGC 3714	11:31:53.59	+28:21:29.3	0.128	—	0.024	Composite	(1)
UGC 06527 NED03	11:32:40.32	+52:57:02.4	—	0.210	0.027	Type 2	(1)
CGCG 126-101	11:34:50.52	+25:31:50.4	0.171	—	0.024	Unknown	—
SBS 1132+579	11:35:24.82	+57:38:59.5	0.099	—	0.029	SF	(1)
SBS 1133+572	11:35:49.09	+56:57:08.8	0.114	0.343	0.051	Type 2	(1)
NGC 3758	11:36:29.20	+21:35:48.1	0.119	0.190	0.030	Type 1	(1)
CGCG 097-022	11:36:39.87	+17:38:35.3	—	0.222	0.027	Composite	(1)
NGC 3781	11:39:03.80	+26:21:40.7	0.073	0.398	0.023	Type 1	(1)
NGC 3800	11:40:13.51	+15:20:32.0	0.320	—	0.011	Unknown	—
NGC 3822	11:42:11.10	+10:16:39.7	0.225	—	0.021	Type 2	(2),(3)
SDSS J114212.21+002004.0	11:42:12.31	+00:20:04.7	0.090	0.378	0.019	SF	(1)
NGC 3839	11:43:54.33	+10:47:06.0	0.183	0.218	0.020	SF	(1)
MRK 0428	11:44:10.96	+37:11:12.5	0.104	0.446	0.042	Composite	(1)
UGC 06732	11:45:33.05	+58:58:40.7	—	0.190	0.010	SF	(14)
NGC 3849	11:45:35.14	+03:13:53.1	0.159	—	0.020	SF	(1)
ARP 248 NED02	11:46:45.28	-03:50:51.4	0.139	0.293	0.017	SF	(10)
NGC 3888	11:47:34.15	+55:58:02.4	0.195	—	0.008	SF	(1)
IC 0737	11:48:27.56	+12:43:38.5	—	0.247	0.014	Composite	(15)
NGC 3934	11:52:12.58	+16:51:06.0	0.106	—	0.013	Unknown	—
NGC 3935	11:52:24.06	+32:24:14.0	—	0.306	0.010	LINER	(1)
UGC 06901	11:55:38.05	+43:02:45.6	0.163	—	0.024	SF	(1)
NGC 3987	11:57:20.93	+25:11:42.9	0.216	—	0.015	Unknown	—
NGC 3994	11:57:36.89	+32:16:39.1	0.258	—	0.010	LINER	(1)
IC 0751	11:58:52.49	+42:34:12.3	—	0.201	0.031	Type 2	(1)

Table 1. (Continued.)

name	RA	DEC	$f_{9\mu m}$	$f_{18\mu m}$	z	type	ref
	j2000	j2000	(Jy)	(Jy)			
UGC 07017	12:02:22.46	+29:51:42.2	0.216	0.213	0.010	SF	(1)
NGC 4045	12:02:42.34	+01:58:37.5	0.241	0.321	0.007	LINER	(1)
NGC 4047	12:02:50.75	+48:38:11.0	0.250	—	0.011	Unknown	—
UGC 07064	12:04:43.30	+31:10:35.8	—	0.186	0.025	Type 2	(1)
CGCG 098-059	12:07:09.55	+16:59:43.7	0.146	0.284	0.022	SF	(1)
NGC 4152	12:10:37.46	+16:01:59.8	—	0.271	0.007	SF	(1)
UGC 07179	12:10:58.08	+63:54:52.7	0.175	—	0.009	Composite	(1)
CGCG 215-050 NED02	12:11:56.48	+40:39:18.5	0.067	0.352	0.023	Unknown	—
NGC 4175	12:12:31.05	+29:10:05.9	0.179	0.265	0.014	Type 2	(16)
NGC 4194	12:14:09.62	+54:31:36.0	0.623	1.934	0.008	Type 1	(1)
PG 1211+143	12:14:17.77	+14:03:12.8	0.089	0.217	0.081	Type 1	(2),(3)
CGCG 013-111	12:14:51.29	-03:29:22.4	—	0.243	0.033	Type 2	(1)
NGC 4226	12:16:26.29	+47:01:32.4	0.124	—	0.024	Unknown	—
IC 0773	12:18:08.09	+06:08:22.4	—	0.257	0.018	Composite	(1)
NGC 4253	12:18:26.54	+29:48:47.2	0.220	0.859	0.013	Composite	(1)
SDSS J121849.71+142458.3	12:18:49.88	+14:24:59.4	1.428	—	0.008	SF	(2)
SDSS J121956.14+052039.5	12:19:56.13	+05:20:39.0	0.600	0.662	0.008	SF	(1)
VCC 0435	12:20:47.22	+17:00:58.3	0.105	0.186	0.026	SF	(1)
NGC 4290	12:20:47.55	+58:05:32.9	0.135	0.281	0.010	SF	(1)
NGC 4332	12:22:46.76	+65:50:37.6	0.189	0.417	0.009	Composite	(1)
NGC 4334	12:23:23.82	+07:28:23.2	0.190	0.254	0.014	SF	(1)
SDSS J122512.25+543019.4	12:25:11.93	+54:30:19.1	0.158	—	0.008	SF	(1)
NGC 4385	12:25:42.75	+00:34:21.8	0.167	0.635	0.007	SF	(4)
NGC 4388	12:25:46.83	+12:39:43.1	0.462	1.589	0.009	Type 2	(1)
NGC 4355	12:26:54.64	-00:52:39.3	0.266	3.286	0.007	Type 2	(3)
NGC 4441	12:27:20.20	+64:48:05.8	—	0.212	0.009	Composite	(1)
KUG 1225+404	12:27:38.00	+40:09:38.2	—	0.220	0.037	Composite	(1)
3C 273	12:29:06.77	+02:03:08.0	0.276	0.454	0.158	Type 1	(2)
NGC 4500	12:31:22.22	+57:57:51.9	0.173	0.320	0.010	SF	(3)
NGC 4495	12:31:22.84	+29:08:11.1	0.205	—	0.015	Composite	(1)
N4532	12:34:19.24	+06:28:08.9	—	0.263	0.007	SF	(2)
NGC 4535	12:34:20.39	+08:11:52.7	0.088	0.276	0.007	SF	(11)
NGC 4536	12:34:27.08	+02:11:18.0	1.018	—	0.006	SF	(11)
NGC 4568	12:36:34.25	+11:14:19.4	0.993	0.914	0.007	SF	(1)
IC 3581	12:36:37.98	+24:25:43.0	—	0.260	0.023	Composite	(1)
KUG 1238+278A	12:40:46.40	+27:33:54.2	—	0.240	0.056	LINER	(1)
WAS 61	12:42:10.68	+33:17:02.8	—	0.222	0.044	Type 1	(1)
MCG +07-26-051	12:46:56.82	+42:16:00.2	0.161	0.219	0.033	Unknown	—

Table 1. (Continued.)

name	RA	DEC	$f_{9\mu m}$	$f_{18\mu m}$	$z$	type	ref
	j2000	j2000	(Jy)	(Jy)			
NGC 4704	12:48:46.46	+41:55:16.7	—	0.227	0.027	Type 2	(3)
2MASX J12494552+4328570	12:49:45.51	+43:28:56.2	—	0.199	0.062	Type 2	(1)
2MASX J12501385+0734443	12:50:13.81	+07:34:44.7	0.098	0.239	0.038	SF	(1)
SHOC 391	12:53:05.97	-03:12:58.7	—	0.298	0.023	Composite	(1)
NGC 4793	12:54:40.94	+28:56:20.7	0.809	—	0.008	SF	(1)
IC 0836	12:55:54.22	+63:36:41.9	0.095	0.151	0.009	Unknown	—
UGC 08058	12:56:14.27	+56:52:25.4	1.051	4.396	0.042	Type 1	(2)
2MASX J13000533+1632151	13:00:05.31	+16:32:14.2	0.088	0.175	0.080	Type 2	(1)
NGC 4922 NED02	13:01:25.28	+29:18:50.4	0.149	0.740	0.023	Type 2	(1)
VV 283a	13:01:50.38	+04:19:58.9	0.107	0.322	0.037	Type 2	(1)
NGC 4963	13:05:52.04	+41:43:18.2	0.101	—	0.024	Unknown	—
UGC 08237	13:08:54.20	+62:18:23.1	0.122	—	0.010	SF	(10)
NGC 5020	13:12:39.88	+12:35:59.8	0.103	—	0.011	SF	(10)
IC 0860	13:15:03.49	+24:37:08.1	—	0.285	0.013	Unknown	—
UGC 08327 NED02	13:15:17.27	+44:24:26.6	0.092	0.264	0.035	LINER	(1)
UGC 08335 NED02	13:15:34.91	+62:07:29.0	0.168	0.853	0.031	Composite	(1)
2MASX J13163979+4452351	13:16:39.69	+44:52:35.3	0.135	0.360	0.091	Type 2	(1)
NGC 5060	13:17:16.22	+06:02:14.4	—	0.189	0.021	Unknown	—
IC 0883	13:20:35.31	+34:08:22.1	0.213	0.554	0.023	Composite	(1)
NGC 5104	13:21:23.11	+00:20:32.7	0.204	0.307	0.019	Composite	(12)
[HB89] 1321+058	13:24:19.88	+05:37:04.4	0.216	0.328	0.203	Type 1	(1)
NGC 5149	13:26:09.16	+35:56:04.5	0.115	0.291	0.019	Composite	(1)
2MASX J13315286+0200596	13:31:52.83	+02:00:59.7	—	0.170	0.086	Type 2	(1)
NGC 5218	13:32:10.30	+62:46:04.1	0.188	0.484	0.010	Composite	(17)
SDSS J133223.99+110620.3	13:32:24.05	+11:06:19.8	0.074	0.282	0.031	SF	(1)
UGC 08561	13:34:57.36	+34:02:39.0	0.174	—	0.024	SF	(1)
[HB89] 1334+246	13:37:18.71	+24:23:02.8	0.449	0.612	0.108	Type 1	(2),(3)
SDSS J133817.27+481632.2	13:38:17.26	+48:16:33.3	0.165	0.556	0.028	Type 2	(1)
NGC 5257	13:39:52.94	+00:50:23.6	0.295	—	0.023	SF	(2)
NGC 5263	13:39:55.56	+28:24:01.5	0.126	—	0.016	SF	(18)
NGC 5258	13:39:57.49	+00:49:48.0	0.299	0.311	0.023	SF	(4)
CGCG 045-068	13:40:27.15	+04:46:24.8	0.075	0.250	0.023	Composite	(1)
IC 0910	13:41:07.82	+23:16:55.3	—	0.265	0.027	LINER	(2)
MRK 0268	13:41:11.09	+30:22:41.0	—	0.211	0.040	Type 1	(1)
MRK 0273:[XXM2002] Radio N	13:44:42.09	+55:53:13.7	0.135	0.871	0.037	Type 2	(1)
MRK 0796	13:46:49.45	+14:24:00.9	0.116	0.429	0.021	Composite	(1)
MRK 1361	13:47:04.36	+11:06:22.5	0.141	0.398	0.023	Type 2	(1)
2MASX J13470695+3456238	13:47:06.98	+34:56:24.9	—	0.239	0.054	Composite	(1)

Table 1. (Continued.)

name	RA	DEC	$f_{9\mu m}$	$f_{18\mu m}$	$z$	type	ref
	j2000	j2000	(Jy)	(Jy)			
4C +12.50	13:47:33.33	+12:17:24.8	—	0.311	0.121	Type 1	(1)
UGC 08728	13:48:12.71	+07:23:42.5	0.115	0.179	0.023	Type 2	(1)
FIRST J134913.9+351525	13:49:14.18	+35:15:23.8	0.251	—	0.017	SF	(18)
NGC 5331 NED01	13:52:16.18	+02:06:05.7	0.192	—	0.033	SF	(19)
PG 1351+640	13:53:15.80	+63:45:45.6	0.108	0.307	0.088	Type 1	(2),(3)
NGC 5347	13:53:17.85	+33:29:26.9	0.138	0.601	0.008	Type 2	(1)
UGC 08827	13:54:31.12	+15:02:39.3	0.160	0.362	0.018	Composite	(1)
MRK 0463E	13:56:02.86	+18:22:18.4	0.376	1.103	0.051	Type 2	(1)
NGC 5383	13:57:04.94	+41:50:47.2	0.262	0.346	0.007	SF	(1)
NGC 5374	13:57:29.66	+06:05:48.0	0.123	—	0.015	SF	(1)
SDSS J135817.50+010843.4	13:58:17.47	+01:08:44.6	—	0.285	0.035	SF	(1)
NGC 5394	13:58:33.65	+37:27:11.8	0.237	0.413	0.012	Composite	(1)
MCG +06-31-036	13:58:41.85	+35:05:15.4	0.105	0.175	0.035	SF	(1)
NGC 5430	14:00:45.78	+59:19:42.5	0.375	0.813	0.010	SF	(1)
NGC 5433	14:02:36.08	+32:30:37.1	0.230	0.360	0.015	SF	(1)
[HB89] 1402+436	14:04:38.68	+43:27:07.3	—	0.254	0.323	Type 1	(1)
VIII Zw 357	14:06:09.50	+02:19:52.8	0.119	0.319	0.025	SF	(1)
NGC 5480	14:06:21.42	+50:43:28.3	0.219	—	0.006	SF	(1)
MRK 0668	14:07:00.43	+28:27:15.0	0.080	0.305	0.077	Type 1	(1)
CGCG 074-129	14:10:41.41	+13:33:28.9	—	0.471	0.016	Type 2	(1)
CGCG 018-077	14:12:15.63	-00:38:00.4	0.091	—	0.026	Unknown	—
NGC 5506	14:13:14.86	-03:12:26.8	0.823	2.240	0.006	Type 2	(1)
NGC 5541	14:16:31.77	+39:35:25.3	0.234	—	0.026	SF	(18)
IC 4395	14:17:20.96	+26:51:26.1	0.119	0.178	0.037	Composite	(1)
NGC 5548	14:17:59.58	+25:08:12.6	0.157	0.409	0.017	Type 1	(1)
UGC 09165	14:18:47.65	+24:56:21.4	0.232	—	0.018	SF	(18)
MRK 1490	14:19:43.20	+49:14:10.8	0.088	0.395	0.026	Composite	(1)
IC 4408	14:21:12.95	+29:59:36.1	0.113	—	0.030	Composite	(1)
SBS 1419+480	14:21:29.78	+47:47:25.3	0.046	0.189	0.073	Type 1	(1)
NGC 5600	14:23:49.39	+14:38:19.7	0.348	—	0.008	Unknown	—
NGC 5610	14:24:22.95	+24:36:51.8	0.167	0.371	0.017	Composite	(1)
NGC 5633	14:27:28.53	+46:08:47.1	0.308	—	0.008	SF	(1)
NGC 5653	14:30:10.29	+31:12:56.3	0.605	0.799	0.012	SF	(21)
NGC 5678:[HK83] 42	14:32:05.06	+57:55:16.8	0.419	—	0.006	SF	(3)
SDSS J143225.99+080448.4	14:32:25.91	+08:04:46.9	0.332	0.513	0.007	SF	(1)
SDSS J143247.74+492751.5	14:32:47.59	+49:27:48.2	—	0.384	0.006	SF	(1)
KUG 1433+353	14:35:18.23	+35:07:08.2	0.134	—	0.029	Composite	(1)
UGC 09412	14:36:22.10	+58:47:39.9	0.188	0.669	0.031	Type 1	(2),(3)

Table 1. (Continued.)

name	RA j2000	DEC j2000	$f_{9\mu m}$ (Jy)	$f_{18\mu m}$ (Jy)	z	type	ref
UGC 09425 NED02	14:37:51.08	+30:28:48.7	—	0.179	0.035	SF	(10)
SDSS J144011.31-001719.5	14:40:11.35	-00:17:22.6	1.010	1.513	0.006	SF	(4)
MRK 0477	14:40:38.11	+53:30:15.8	—	0.352	0.038	Type 2	(1)
2MASX J14410437+5320088	14:41:04.38	+53:20:09.5	—	0.205	0.105	Type 2	(1)
2MASX J14492067+4221013	14:49:20.75	+42:21:00.6	0.093	0.162	0.179	Type 1	(1)
NGC 5765B	14:50:51.45	+05:06:52.2	0.147	0.408	0.028	Type 2	(1)
UGC 09561 NOTES01	14:51:29.35	+09:20:05.2	0.114	0.164	0.029	Composite	(1)
N5795	14:56:19.32	+49:23:55.2	0.153	—	0.008	Unknown	—
UGC 09618 NED02	14:57:00.69	+24:37:04.5	0.240	0.289	0.034	SF	(22)
NGC 5804	14:57:06.90	+49:40:09.5	0.115	0.108	0.013	Type 1	(1)
NGC 5792	14:58:22.67	-01:05:28.1	0.330	0.472	0.006	SF	(23)
UGC 09639	14:58:36.05	+44:53:00.6	0.158	0.297	0.036	Type 2	(1)
CGCG 105-099	15:02:53.23	+16:55:09.0	—	0.263	0.021	Composite	(1)
MRK 0841	15:04:01.21	+10:26:15.6	0.126	0.372	0.036	Type 1	(2),(3)
2MASX J15051788+0809127	15:05:17.93	+08:09:13.4	—	0.188	0.039	Composite	(1)
NGC 5860 NED01	15:06:33.57	+42:38:25.6	0.093	—	0.018	SF	(1)
VV 059a	15:08:05.69	+34:23:21.3	0.096	—	0.046	Unknown	—
CGCG 077-021	15:09:08.72	+09:02:20.1	—	0.228	0.044	SF	(3)
NGC 5875	15:09:12.93	+52:31:41.0	0.164	—	0.012	Type 2	(1)
2MASX J15114125+0518089	15:11:41.28	+05:18:08.4	—	0.249	0.085	Type 1	(1)
CGCG 049-057	15:13:13.21	+07:13:32.7	—	0.179	0.013	Composite	(24)
NGC 5900	15:15:05.29	+42:12:35.0	0.343	0.385	0.008	Unknown	—
NGC 5905	15:15:23.45	+55:31:03.3	0.133	0.137	0.011	SF	(3)
SDSS J151548.37+200121.5	15:15:48.36	+20:01:22.2	0.066	0.181	0.036	SF	(1)
2MASSi J1516532+190048	15:16:53.25	+19:00:47.8	0.102	—	0.190	Type 1	(2),(3)
VV 705 NED01	15:18:06.13	+42:44:44.5	0.156	0.645	0.040	Composite	(1)
SBS 1517+522	15:19:07.47	+52:06:06.9	—	0.182	0.138	Type 1	(1)
SDSS J151947.03+394534.8	15:19:47.07	+39:45:36.4	—	0.266	0.047	SF	(1)
SDSS J152238.10+333135.8	15:22:38.05	+33:31:35.2	—	0.194	0.125	Composite	(1)
2MASX J15234787+2855032	15:23:47.83	+28:55:02.4	—	0.227	0.087	Type 1	(1)
NGC 5930	15:26:07.88	+41:40:33.7	0.227	0.782	0.009	Composite	(1)
CGCG 021-096	15:26:37.63	+00:35:32.6	0.065	0.220	0.051	Type 2	(1)
IRAS 15250+3609	15:26:59.46	+35:58:37.2	0.098	0.452	0.055	Composite	(1)
NGC 5936	15:30:00.85	+12:59:20.2	0.386	0.663	0.013	Composite	(1)
NGC 5937	15:30:46.17	-02:49:44.9	0.597	0.843	0.009	SF	(16)
2MASX J15322966+3007490	15:32:29.78	+30:07:48.4	—	0.222	0.065	Type 2	(1)
NGC 5953	15:34:32.36	+15:11:37.5	0.408	0.580	0.007	Type 2	(3)
NGC 5954	15:34:35.07	+15:12:00.8	0.197	0.299	0.006	SF	(1)



Table 1. (Continued.)

name	RA	DEC	$f_{9\mu m}$	$f_{18\mu m}$	$z$	type	ref
	j2000	j2000	(Jy)	(Jy)			
ARP 220:[LDT2006] E13	15:34:57.24	+23:30:11.6	0.249	2.261	0.018	Type 1	(1)
NGC 5962	15:36:31.80	+16:36:27.0	0.366	—	0.007	Unknown	—
SDSS J153927.51+245651.4	15:39:27.49	+24:56:51.0	—	0.235	0.023	SF	(3)
NGC 5975	15:39:57.95	+21:28:13.2	0.166	0.188	0.015	Type 2	(1)
NGC 5980	15:41:30.49	+15:47:18.9	0.274	—	0.014	Unknown	—
CGCG 166-047	15:43:57.35	+28:31:26.5	—	0.180	0.032	Type 2	(1)
NGC 5990	15:46:16.41	+02:24:55.3	0.450	0.802	0.012	SF	(1)
UGC 10029	15:46:54.32	+05:53:27.7	0.097	0.196	0.042	Unknown	—
UGC 10070	15:51:12.88	+47:15:17.6	0.255	0.327	0.019	Unknown	—
MRK 0492	15:58:43.72	+26:49:04.2	0.092	0.370	0.014	Composite	(1)
NGC 6052 NED01	16:05:12.93	+20:32:35.4	0.200	0.397	0.016	SF	(1)
GIN 510	16:07:38.49	+18:28:51.1	—	0.176	0.037	Composite	(1)
IC 1198	16:08:36.37	+12:19:49.8	—	0.246	0.034	Type 1	(1)
2MASX J16094822+0434525	16:09:48.24	+04:34:52.8	—	0.248	0.064	Type 2	(1)
NGC 6090 NED02	16:11:40.77	+52:27:27.0	0.196	0.499	0.029	SF	(1)
UGC 10322	16:18:07.93	+22:13:32.3	0.183	—	0.015	SF	(1)
NGC 6120	16:19:48.05	+37:46:28.5	0.164	0.270	0.031	SF	(25)
SBS 1620+504	16:22:17.74	+50:22:20.1	0.116	0.164	0.057	Composite	(1)
UGC 10384	16:26:46.63	+11:34:49.9	0.122	—	0.017	SF	(1)
SN 1951I	16:32:20.81	+19:49:32.8	—	0.556	0.008	SF	(11)
SDSS J163425.28+213228.5	16:34:25.37	+21:32:27.7	0.162	0.201	0.010	SF	(1)
FBQS J164018.1+384220	16:40:18.18	+38:42:20.4	—	0.233	0.020	PN	(2),(3)
3C 345	16:42:58.88	+39:48:37.2	0.102	0.353	0.593	Type 1	(2),(3)
NGC 6247	16:48:20.30	+62:58:36.5	0.233	0.289	0.015	SF	(1)
2MASX J16512188+2155264	16:51:21.89	+21:55:26.5	0.119	—	0.055	Type 2	(1)
NGC 6306	17:07:36.90	+60:43:43.1	0.095	0.232	0.010	SF	(10)
NGC 6361	17:18:41.14	+60:36:28.6	0.266	—	0.013	Unknown	—
2MASX J17380143+5613257	17:38:01.37	+56:13:26.2	0.070	0.241	0.065	Type 2	(1)
MCG -01-53-004	20:45:14.66	-05:29:03.1	—	0.337	0.027	Composite	(1)
NGC 6967	20:47:34.10	+00:24:40.0	—	0.285	0.013	Type 2	(2),(3)
UGC 11763	21:32:27.84	+10:08:18.8	0.134	0.236	0.063	Type 1	(2),(3)
2MASX J21522605-0810248	21:52:26.05	-08:10:25.7	—	0.324	0.035	Type 2	(1)
UGC 11865	21:58:36.01	+12:02:20.6	0.142	0.197	0.031	SF	(26)
NGC 7189	22:03:16.00	+00:34:15.5	—	0.197	0.030	Type 2	(1)
CGCG 429-014	22:37:07.77	+14:13:52.8	0.116	—	0.038	Composite	(1)
NGC 7364	22:44:24.39	-00:09:41.1	0.106	—	0.016	Unknown	—
2MASX J22533299-0024428	22:53:32.93	-00:24:42.0	—	0.311	0.058	Composite	(1)
IC 1464B	23:03:11.18	-08:59:23.6	0.118	0.231	0.024	SF	(26),(27)

**Table 1.** (Continued.)

name	RA	DEC	$f_{9\mu m}$	$f_{18\mu m}$	$z$	type	ref
	j2000	j2000	(Jy)	(Jy)			
MRK 0926	23:04:43.62	-08:41:09.1	0.060	0.214	0.047	Type 1	(1)
UGC 12348	23:05:18.79	+00:11:23.1	0.114	0.172	0.025	Type 2	(3)
NGC 7580	23:17:36.44	+14:00:04.9	0.137	—	0.015	SF	(1)
NGC 7603	23:18:56.68	+00:14:37.5	0.295	0.321	0.030	Type 1	(2),(3)
UGC 12633	23:30:13.70	+15:45:40.3	0.127	0.190	0.014	Composite	(1)
NGC 7738	23:44:02.07	+00:31:00.5	0.128	0.264	0.023	SF	(4)
2MASX J23470918+1535487	23:47:09.19	+15:35:48.5	—	0.571	0.026	Type 2	(2)

(1) SDSS; (2) SIMBD; (3) NED; (4) Kewley et al. (2006); (5) Kirhakos, S. D., & Steiner, J. E. (1990); (6) Clavel et al. (2000); (7) Parra et al. (2010); (8) Corbett et al. (2003); (9) Burlon et al. (2011); (10) Wang et al. (2009); (11) Ho et al. (1997); (12) Veilleux et al. (1995); (13) Cohen (1992); (14) Bukhmastova (2001); (15) Konstantopoulos et al. (2012); (16) Koulouridis et al. (2006); (17) Yuan et al. (2010); (18) Leech et al. (1989); (19) Wu et al. (1998); (20) Petrosian et al. (2007); (21) Petrosian et al. (2008); (22) Moustakas et al. (2006); (23) Veron-Cetty et al. (1986); (24) Alonso-Herrero et al. (2012); (25) Poggianti et al. (2000); (26) Okayama obs.; (27) Caccianiga et al. (2000)

**Table 2.** Summary of the classification types of 243 galaxies for the 9  $\mu m$  LF and 255 galaxies for the 18  $\mu m$  LF.

type	9 $\mu m$ (percentage)	18 $\mu m$ (percentage)
Type 1	25 (10.3%)	41 (16.0%)
Type 2	39 (15.6%)	64 (25.0%)
LINER	6 (2.5%)	11 (4.3%)
Composite	50 (20.6%)	57 (22.3%)
SF	95 (39.5%)	71 (28.1%)
Unknown	28 (11.5%)	11 (4.3%)
All	243 (100%)	255 (100%)

**Table 3.** LF of all galaxies at 9 and 18  $\mu\text{m}$ .

log $L$ [ $L_{\odot}$ ]	9 $\mu\text{m}$			18 $\mu\text{m}$		
	$\phi$ [ $\text{Mpc}^{-3} \text{Mag}^{-1}$ ]	1 $\sigma$ err [ $\text{Mpc}^{-3} \text{Mag}^{-1}$ ]	N	$\phi$ [ $\text{Mpc}^{-3} \text{Mag}^{-1}$ ]	1 $\sigma$ err [ $\text{Mpc}^{-3} \text{Mag}^{-1}$ ]	N
9.00	$5.76 \times 10^{-4}$	$1.89 \times 10^{-4}$	12	$7.61 \times 10^{-4}$	$2.09 \times 10^{-4}$	15
9.40	$6.06 \times 10^{-4}$	$9.37 \times 10^{-5}$	50	$3.07 \times 10^{-4}$	$6.35 \times 10^{-5}$	28
9.80	$1.76 \times 10^{-4}$	$2.35 \times 10^{-5}$	64	$1.34 \times 10^{-4}$	$2.07 \times 10^{-5}$	50
10.2	$5.07 \times 10^{-5}$	$6.94 \times 10^{-6}$	59	$4.72 \times 10^{-5}$	$6.29 \times 10^{-6}$	65
10.6	$9.85 \times 10^{-6}$	$1.64 \times 10^{-6}$	40	$8.81 \times 10^{-6}$	$1.44 \times 10^{-6}$	41
11.0	$3.11 \times 10^{-7}$	$1.58 \times 10^{-7}$	4	$1.77 \times 10^{-6}$	$3.45 \times 10^{-7}$	29
11.4	$1.14 \times 10^{-7}$	$4.84 \times 10^{-8}$	6	$1.95 \times 10^{-7}$	$5.88 \times 10^{-8}$	12
11.8	$1.99 \times 10^{-8}$	$9.84 \times 10^{-9}$	5	$3.88 \times 10^{-8}$	$1.45 \times 10^{-8}$	8
12.2	$2.56 \times 10^{-9}$	$1.84 \times 10^{-9}$	2	$5.31 \times 10^{-9}$	$3.11 \times 10^{-9}$	3
12.6	—	—	—	$7.74 \times 10^{-10}$	$5.70 \times 10^{-10}$	2
13.4	$1.30 \times 10^{-10}$	$1.30 \times 10^{-10}$	1	$1.42 \times 10^{-10}$	$1.01 \times 10^{-10}$	2

**Table 4.** Best double-power law fit parameters for the 9 and 18  $\mu\text{m}$  LFs

band	$\phi^*$ ( $\text{Mpc}^{-3} \text{Mag}^{-1}$ )	$L^*$ ( $L_{\odot}$ )	$\alpha$ (faint-end)	$\beta$ (bright-end)
9 $\mu\text{m}$	$(1.7 \pm 0.9) \times 10^{-4}$	$(1.2 \pm 0.4) \times 10^{10}$	$-0.6 \pm 0.2$	$-2.6 \pm 0.2$
18 $\mu\text{m}$	$(1.0 \pm 0.8) \times 10^{-4}$	$(1.4 \pm 0.7) \times 10^{10}$	$-0.7 \pm 0.2$	$-2.1 \pm 0.2$

**Table 5.**  $9\ \mu\text{m}$  LF for various spectroscopic galaxies.

$\log L$	Type 1 AGN			Type 2 AGN		
	$\phi$	$1\sigma$ err	N	$\phi$	$1\sigma$ err	N
	$[L_{\odot}]$	$[\text{Mpc}^{-3} \text{Mag}^{-1}]$		$[\text{Mpc}^{-3} \text{Mag}^{-1}]$	$[\text{Mpc}^{-3} \text{Mag}^{-1}]$	
9.00	—	—		$3.28 \times 10^{-5}$	$3.28 \times 10^{-5}$	1
9.40	$7.03 \times 10^{-6}$	$7.03 \times 10^{-6}$	1	$3.06 \times 10^{-5}$	$1.87 \times 10^{-5}$	3
9.80	$8.54 \times 10^{-6}$	$5.12 \times 10^{-6}$	3	$2.83 \times 10^{-5}$	$9.64 \times 10^{-6}$	9
10.2	$2.73 \times 10^{-6}$	$1.41 \times 10^{-6}$	4	$8.85 \times 10^{-6}$	$2.79 \times 10^{-6}$	11
10.6	$1.81 \times 10^{-6}$	$6.80 \times 10^{-7}$	8	$1.86 \times 10^{-6}$	$6.88 \times 10^{-7}$	8
11.0	$5.37 \times 10^{-8}$	$5.37 \times 10^{-8}$	1	$1.69 \times 10^{-7}$	$1.20 \times 10^{-7}$	2
11.4	$3.71 \times 10^{-8}$	$2.84 \times 10^{-8}$	2	$5.57 \times 10^{-8}$	$3.30 \times 10^{-8}$	3
11.8	$9.47 \times 10^{-9}$	$5.62 \times 10^{-9}$	3	$1.05 \times 10^{-8}$	$8.07 \times 10^{-9}$	2
12.2	$2.56 \times 10^{-9}$	$1.84 \times 10^{-9}$	2	—	—	
13.4	$1.30 \times 10^{-10}$	$1.32 \times 10^{-10}$	1	—	—	
$\log L$	LINER			Star-Forming		
	$\phi$	$1\sigma$ err	N	$\phi$	$1\sigma$ err	N
	$[L_{\odot}]$	$[\text{Mpc}^{-3} \text{Mag}^{-1}]$		$[\text{Mpc}^{-3} \text{Mag}^{-1}]$	$[\text{Mpc}^{-3} \text{Mag}^{-1}]$	
9.00	—	—		$3.39 \times 10^{-4}$	$1.47 \times 10^{-4}$	7
9.40	$2.23 \times 10^{-5}$	$2.23 \times 10^{-5}$	1	$3.54 \times 10^{-4}$	$7.42 \times 10^{-5}$	27
9.80	$6.71 \times 10^{-6}$	$5.05 \times 10^{-6}$	2	$7.74 \times 10^{-5}$	$1.53 \times 10^{-5}$	29
10.2	$1.87 \times 10^{-6}$	$1.46 \times 10^{-6}$	2	$2.17 \times 10^{-5}$	$4.61 \times 10^{-6}$	24
10.6	$1.66 \times 10^{-7}$	$1.66 \times 10^{-7}$	1	$2.38 \times 10^{-6}$	$8.68 \times 10^{-7}$	8
$\log L$	Composite			Unknown		
	$\phi$	$1\sigma$ err	N	$\phi$	$1\sigma$ err	N
	$[L_{\odot}]$	$[\text{Mpc}^{-3} \text{Mag}^{-1}]$		$[\text{Mpc}^{-3} \text{Mag}^{-1}]$	$[\text{Mpc}^{-3} \text{Mag}^{-1}]$	
9.00	$9.43 \times 10^{-5}$	$9.43 \times 10^{-5}$	1	$1.10 \times 10^{-4}$	$6.43 \times 10^{-5}$	3
9.40	$1.23 \times 10^{-4}$	$4.18 \times 10^{-5}$	10	$6.90 \times 10^{-5}$	$2.50 \times 10^{-5}$	8
9.80	$3.09 \times 10^{-5}$	$9.63 \times 10^{-6}$	12	$2.44 \times 10^{-5}$	$8.92 \times 10^{-6}$	9
10.2	$1.05 \times 10^{-5}$	$3.05 \times 10^{-6}$	13	$5.13 \times 10^{-6}$	$2.39 \times 10^{-6}$	5
10.6	$2.84 \times 10^{-6}$	$8.67 \times 10^{-7}$	12	$7.93 \times 10^{-7}$	$4.59 \times 10^{-7}$	3
11.0	$8.84 \times 10^{-8}$	$8.84 \times 10^{-8}$	1	—	—	
11.4	$2.11 \times 10^{-8}$	$2.11 \times 10^{-8}$	1	—	—	

**Table 6.** 18  $\mu\text{m}$  LF for various spectroscopic galaxies.

log $L$ [ $L_{\odot}$ ]	Type 1 AGN			Type 2 AGN		
	$\phi$ [ $\text{Mpc}^{-3} \text{Mag}^{-1}$ ]	$1\sigma$ err [ $\text{Mpc}^{-3} \text{Mag}^{-1}$ ]	N	$\phi$ [ $\text{Mpc}^{-3} \text{Mag}^{-1}$ ]	$1\sigma$ err [ $\text{Mpc}^{-3} \text{Mag}^{-1}$ ]	N
9.40	—	—		$4.99 \times 10^{-5}$	$2.41 \times 10^{-5}$	5
9.80	$2.92 \times 10^{-6}$	$2.07 \times 10^{-6}$	2	$3.06 \times 10^{-5}$	$9.84 \times 10^{-6}$	12
10.2	$5.10 \times 10^{-6}$	$1.91 \times 10^{-6}$	8	$9.32 \times 10^{-6}$	$2.71 \times 10^{-6}$	13
10.6	$1.71 \times 10^{-6}$	$6.08 \times 10^{-7}$	9	$2.45 \times 10^{-6}$	$7.34 \times 10^{-7}$	12
11.0	$3.48 \times 10^{-7}$	$1.53 \times 10^{-7}$	6	$7.52 \times 10^{-7}$	$2.18 \times 10^{-7}$	13
11.4	$1.12 \times 10^{-7}$	$4.76 \times 10^{-8}$	6	$5.86 \times 10^{-8}$	$2.98 \times 10^{-8}$	4
11.8	$1.93 \times 10^{-8}$	$9.06 \times 10^{-9}$	5	$1.95 \times 10^{-8}$	$1.13 \times 10^{-8}$	3
12.2	$3.17 \times 10^{-9}$	$2.26 \times 10^{-9}$	2	$2.13 \times 10^{-9}$	$2.13 \times 10^{-9}$	1
12.6	$5.01 \times 10^{-10}$	$5.01 \times 10^{-10}$	1	$2.72 \times 10^{-10}$	$2.72 \times 10^{-10}$	1
13.4	$1.42 \times 10^{-10}$	$1.01 \times 10^{-10}$	2	—	—	
<hr/>						
log $L$ [ $L_{\odot}$ ]	LINER			Star-Forming		
	$\phi$ [ $\text{Mpc}^{-3} \text{Mag}^{-1}$ ]	$1\sigma$ err [ $\text{Mpc}^{-3} \text{Mag}^{-1}$ ]	N	$\phi$ [ $\text{Mpc}^{-3} \text{Mag}^{-1}$ ]	$1\sigma$ err [ $\text{Mpc}^{-3} \text{Mag}^{-1}$ ]	N
9.00	$4.48 \times 10^{-5}$	$4.48 \times 10^{-5}$	1	$6.00 \times 10^{-4}$	$1.82 \times 10^{-4}$	12
9.40	$9.68 \times 10^{-6}$	$9.68 \times 10^{-6}$	1	$1.59 \times 10^{-4}$	$5.00 \times 10^{-5}$	12
9.80	$4.17 \times 10^{-6}$	$2.98 \times 10^{-6}$	2	$5.83 \times 10^{-5}$	$1.39 \times 10^{-5}$	20
10.2	$9.80 \times 10^{-7}$	$7.08 \times 10^{-7}$	2	$1.58 \times 10^{-5}$	$3.76 \times 10^{-6}$	20
10.6	$8.55 \times 10^{-7}$	$4.97 \times 10^{-7}$	3	$1.27 \times 10^{-6}$	$5.36 \times 10^{-7}$	6
11.0	$1.51 \times 10^{-7}$	$1.06 \times 10^{-7}$	2	$6.00 \times 10^{-8}$	$6.00 \times 10^{-8}$	1
<hr/>						
log $L$ [ $L_{\odot}$ ]	Composite			Unknown		
	$\phi$ [ $\text{Mpc}^{-3} \text{Mag}^{-1}$ ]	$1\sigma$ err [ $\text{Mpc}^{-3} \text{Mag}^{-1}$ ]	N	$\phi$ [ $\text{Mpc}^{-3} \text{Mag}^{-1}$ ]	$1\sigma$ err [ $\text{Mpc}^{-3} \text{Mag}^{-1}$ ]	N
9.00	$1.16 \times 10^{-4}$	$9.11 \times 10^{-5}$	2	—	—	
9.40	$6.67 \times 10^{-5}$	$2.48 \times 10^{-5}$	8	$2.15 \times 10^{-5}$	$1.57 \times 10^{-5}$	2
9.80	$2.84 \times 10^{-5}$	$9.47 \times 10^{-6}$	11	$9.41 \times 10^{-6}$	$5.94 \times 10^{-6}$	3
10.2	$1.30 \times 10^{-5}$	$3.37 \times 10^{-6}$	18	$2.91 \times 10^{-6}$	$1.58 \times 10^{-6}$	4
10.6	$2.06 \times 10^{-6}$	$7.26 \times 10^{-7}$	9	$4.70 \times 10^{-7}$	$3.34 \times 10^{-7}$	2
11.0	$4.64 \times 10^{-7}$	$1.82 \times 10^{-7}$	7	—	—	
11.4	$2.42 \times 10^{-8}$	$1.73 \times 10^{-8}$	2	—	—	

**Table 7.** Comparison of the number density ratio of Type 2 to Type 1 AGNs ( $\Phi_{\text{Type2}}/\Phi_{\text{Type1}}$ ) with some previous studies.

$\Phi_{\text{Type2}}(L \geq 10^{10}L_{\odot}) / \Phi_{\text{Type1}}(L \geq 10^{10}L_{\odot})$	wavelength	reference
$\sim 1.63$	15-55 keV	Burlon et al. (2011)
$\sim 1.75$	12 $\mu\text{m}$	Rush et al. (1993)
$1.73 \pm 0.36$	18 $\mu\text{m}$	This work
$\sim 0.67$	[OIII]	Hao et al. (2005b)